# A Quantum Molecular Movie: Polyad Predissociation Dynamics in the VUV Excited $3p\delta\,^2\Sigma_u$ state of $NO_2$

# Journal Name

## ARTICLE TYPE

# A Quantum Molecular Movie: Polyad Predissociation Dynamics in the VUV Excited $3p\sigma^2\Sigma_u$ state of NO2

Varun Makhija,[a,b] Andrey E. Boguslavskiy,[b,d] Ruaridh Forbes,[b,c] Kevin Veyrinas,[b] Iain Wilkinson,[e] Rune Lausten,[d] Michael S. Schuurman,[d,f] Edward R. Grant,[g] and Albert Stolow[b,d,f,†]

The optical formation of coherent superposition states, a wavepacket, can allow the study of zeroth-order states, the evolution of which exhibit structural and electronic changes as a function of time: this leads to the notion of a molecular movie. Intramolecular vibrational energy redistribution, due to anharmonic coupling between modes, is the molecular movie considered here. There is no guarantee, however, that the formed superposition will behave semi-classically (e.g. Gaussian wavepacket dynamics) or even as an intuitively useful zeroth-order state. Here we present Time-Resolved Photoelectron Spectroscopy (TRPES) studies of an electronically excited triatomic molecule wherein the vibrational dynamics must be treated quantum mechanically and the simple picture of population flow between coupled normal modes fails. Specifically, we report on vibronic wavepacket dynamics in the zeroth-order $3p\sigma^2\Sigma_u$ Rydberg state of NO2. This wavepacket exemplifies two general features of excited state dynamics in polyatomic molecules: anharmonic multimodal vibrational coupling (forming polyads); nonadiabatic coupling between nuclear and electronic coordinates, leading to predissociation. The latter suggests that the polyad vibrational states in the zeroth-order 3p Rydberg manifold are quasi-bound and best understood to be scattering resonances. We observed a rapid dephasing of an initially prepared 'bright' valence state into the relatively long-lived 3p Rydberg state whose multimodal vibrational dynamics and decay we monitor as a function of time. Our quantum simulations, based on an effective spectroscopic Hamiltonian, describe the essential features of the multimodal Fermi resonance-driven vibrational dynamics in the 3p state. We also present evidence of polyad-specificity in the state-dependent predissociation rates, leading to free atomic and molecular fragments. We emphasize that a Quantum Molecular Movie is required to visualize wavepacket dynamics in the $3p\sigma^2\Sigma_u$ Rydberg state of NO2.

[a] Department of Chemistry and Physics, University of Mary Washington, Fredericksburg, VA 22401, United States

[b] Department of Physics, University of Ottawa, 150 Louis Pasteur, Ottawa, ON, K1N 6N5, Canada

[c] SLAC National Accelerator Laboratory, 2575 Sand Hill Rd, Menlo Park, California 94025, USA

[d] National Research Council Canada, 100 Sussex Drive, Ottawa, ON, K1N 5A2, Canada

[e] Locally-Sensitive Time-Resolved Spectroscopy, Helmholtz-Zentrum Berlin für Materialien und Energie, Hahn-Meitner-Platz 1, 14109 Berlin, Germany

[f] Department of Chemistry, University of Ottawa, 150 Louis Pasteur, Ottawa, ON, K1N 6N5, Canada

[g] Department of Chemistry, University of British Columbia, Vancouver, British Columbia, Canada V6T 1Z3

[†] Email: astolow@uottawa.ca

# 1   Introduction

Wavepackets are by definition coherent superpositions of quantum states, typically prepared by ultrashort optical pulses. They are of great utility because the superposition of "exact" (i.e. no approximations) molecular eigenstates — which in general are extremely complicated — constructs, for a short period of time, a zeroth-order state which is a solution to a simpler Hamiltonian[1]. The 'optically constructed' zeroth-order state will be time dependent, since it is by definition not a solution to the Schrodinger equation for the exact Hamiltonian. However, by monitoring the time evolution of the zeroth-order states, one may learn about the terms in the Hamiltonian which were neglected. An example relevant to this Faraday Discussion is the coherent superposition of exact non-Born-Oppenheimer molecular eigenstates which, for a short period of time, may behave like an adiabatic Born-Oppenheimer state having well defined but transient electronic character, the time dependence of which sheds light on nonadiabatic couplings. By analogy, on attosecond time scales, a coherent superposition of exact n-body electronic states may behave, for a very short period of time, like a molecular orbital (a single particle wavefunction), the time dependence of which informs about electron correlation. An example directly relevant to the present submission is a coherent superposition of exact (anharmonic, coupled) vibrational eigenstates which, for a short period of time, may behave like a (harmonic) normal mode or perhaps a local mode (single bond excitation). In some cases, famously so for the harmonic oscillator, the coherent superposition of eigenstates may even exhibit classical localization. This can be highly instructive because classical trajectories often provide far greater insight into molecular dynamics than do the structure of the molecular eigenstates. This attractive idea leads to the simple picture of a localized wavepacket (e.g. a Gaussian or set of Gaussians) propagating in trajectory-like fashion on a potential surface, undergoing various couplings as a function of time[2]. More generally, the wavepacket picture leads to the notion of structural dynamics, the "visualization of electronic and geometric structural changes as a function of time"[3]. The physical visualization of structural dynamics has compellingly been called a 'molecular movie'[4]. The structural dynamics perspective has been dramatically advanced by time-resolved diffraction studies of wavepacket dynamics in molecules[5–9].

In this Faraday Discussion paper, we revisit the molecular movie concept through the example of excited state wavepacket dynamics in the smallest of polyatomic molecules, a triatomic. Whatever the choice of observable, exact molecular eigenstates are fully quantum mechanical non-separable states often containing complex nodal structure and exhibiting non-classical behaviour. In general, there is no guarantee that a coherent superposition of exact eigenstates will exhibit classical localization or behave like an intuitively useful zeroth order state exhibiting structural changes as a function of time. The molecular movie may be, in general, a quantum movie. Here we present an example of just such a case: vibronic (i.e. vibrational-electronic) wavepacket dynamics in an electronically excited Rydberg state of the canonical triatomic molecule $NO_2$. Our particular focus is on the strong Fermi resonance coupling and complete breakdown of the normal mode picture of vibrational dynamics in this excited state. Furthermore, the $NO_2$ excited state under study also undergoes coupling to dissociation channels, forming atomic and molecular fragments. Below, we provide a brief introduction, with some references, to intramolecular vibrational energy redistribution and predissociation dynamics. In the state of $NO_2$ considered here, the wavepacket picture of vibrational energy flow as a 'structure' traversing and spreading on an anharmonic potential energy surface does not apply. The coherent vibrational (or vibronic) wavepacket dynamics, however, will always be correctly described quantum mechanically and begets the title of this submission.

## 1.1   Polyad Scattering Resonances

The intramolecular vibrational energy redistribution (IVR) dynamics of excited polyatomic molecules has long been an important subject of investigation[10–14]. The literature on IVR is vast, containing numerous important contributions which regretfully cannot be summarized here. Many studies focused on the disentangling of couplings which lead to deviations from the behavior of a multidimensional harmonic oscillator[15–18]. An understanding of these couplings may lead, in restricted cases (*vide infra*), to the physically intuitive picture of IVR being viewed as population flow amongst the normal modes as a function of time. In electronically excited states, IVR is amongst the primary factors driving photochemical dynamics[19–22]. The understanding developed over the years owes much to fundamental frequency and time domain studies of prototypical cases in which the intramolecular dynamics is mediated by a relatively small number of discernible mechanisms, allowing elucidation of their specific contributions to the dynamics[22,23]. Of primary importance amongst these mechanisms is the Fermi resonance coupling between stretching and bending vibrational modes.

IVR would not exist were potential energy surfaces perfectly harmonic, since the normal modes form a complete orthonormal basis. In reality, anharmonicities play a huge role in molecular dynamics: in the harmonic approximation, a bond could never break and chemistry would not exist, pleasing at least some. The simplest example of an anharmonic coupling is the Fermi dyad, exemplified by stretch-bend coupling in the molecule $CO_2$ and arises because, in the ground electronic state, two quanta of the bend are degenerate with one quantum of the symmetric stretch[24–27]. These degenerate states couple to form new states which are of mixed stretch-bend character. The coherent superposition of the two states forming the Fermi dyad may be visualized as periodic vibrational energy flow between stretch and bend, with the period inversely related to the strength of the coupling. The higher-lying vibrational states of polyatomic molecules will typically be strongly mixed by multimodal anharmonic resonance couplings. The notion of normal modes disappears and the assignment of quantum numbers becomes challenging. In the higher energy, high vibrational state density limit, so-called statistical IVR is achieved and the eigenstate level spacing statistics become random. A vibrational wavepacket prepared in the statistical IVR case will exhibit no revivals (at least on experimental time scales). In the case of restricted IVR, a smaller

number of strongly coupled molecular eigenstates may result in clusters of 'bright' states with energy gaps between these. A vibrational wavepacket prepared in this restricted IVR case will exhibit some coherent oscillations with central frequencies related to the energy gaps between clusters and dephasing times related to the energy widths of the clusters[28,29]. This can occur, for example, when the ratios of vibrational frequencies are approximately integers and the couplings may still be treated by perturbation theory, leading to a global pattern of multimodal anharmonic resonances[30]. The blocks of eigenstates states thus formed are termed Fermi polyads, or in the following, polyads. Polyad eigenstates are highly mixed zeroth-order states (i.e. normal modes) which may be assigned approximate polyad quantum numbers[15]. The polyad quantum numbers will be linear combinations of normal mode quantum numbers. This is analogous to block diagonalization where the dimensionality of the block is given by the number of coupled zeroth-order modes.

Time domain studies of IVR in electronically excited states, beginning with the work of Felker and Zewail[19,28,29,31,32], have proved particularly powerful. Following this, Time-Resolved Photoelectron Spectroscopy (TRPES)[33] was used to study the dynamics of IVR in electronically excited states [22,34–37]. The vibrational wavepacket dynamics picture which emerged is that an initially excited zeroth-order 'bright' state couples via anharmonic vibrational (e.g. Fermi resonance) or rovibrational (e.g. Coriolis) effects to otherwise 'dark' zeroth-order bath states. As discussed above, the sets of bright and dark-zeroth order states are understood to be 'optically constructed' from coherent superpositions of initially photoexcited exact molecular eigenstates. In electronically excited states, however, other important processes can play a critical role. First and foremost are electronically nonadiabatic dynamics, ubiquitous in excited polyatomic molecules[38–41]. The dimensionality of the strong nonadiabatic coupling region is 3N-8, two less than the total vibrational degrees of freedom, meaning that two internal degrees of freedom locally (and linearly) lift the electronic degeneracy and have the topography of a double cone: the crossing is thus termed a conical intersection[42,43]. The combination of *ab initio* quantum dynamics with TRPES has led to much progress in the study of dynamics at conical intersections[44–48], recently reviewed in reference[49].

The other fundamentally important excited state process is that of photodissociation[50]. In photodissociation dynamics, the quantum states formed by absorption of light are continuum states and the appropriate description is that of scattering theory[51–53]. In some cases, the electronic transition is to an unbound (repulsive) electronically excited state from which the photodissociation products appear directly and rapidly. Correspondingly, such electronic states have featureless, diffuse electronic absorption spectra. In other cases, the dissociation continuum is not directly accessed by the 'bright' zeroth-order electronic state, but is rather coupled to it via nonadiabatic processes. In this case, depending on the strength of the coupling, the absorption spectrum may still show discernible features (e.g. vibrational progressions) but lineshapes will be broadened due to coupling to the continuum. This process is known as predissociation[54]. In predissociation, the excited state eigenstates prepared by absorption of light should be thought of as compound scattering resonances whose level spacings and widths determines the absorption spectrum and excited state lifetime.

For the case of wavepacket predissociation dynamics, the excited state wavepacket should be thought of as a coherent superposition of scattering resonances. In the weak coupling limit, these may appear resolved in the absorption spectrum but with state-dependent widths (decay lifetimes). The corresponding wavepacket, being the coherent superposition of these, will simultaneously undergo oscillations (beats) and decay. For the case of predissociation in diatomics, coherent wavepacket dynamics were studied experimentally and theoretically for the famous case of IBr[55]. In the absence of predissociation, the excited state wavepacket would undergo persistent oscillations. In IBr, analysis of the wavepacket dynamics showed that the quantum beats both dephased and decayed. The excited state wavepacket in IBr also showed interesting energy-dependent interferences between adiabatic and diabatic wavepackets, leading to an appealing time-domain picture of the origin of the state-dependent scattering resonance linewidths. Such phenomena are, of course, expected to appear in the electronically excited states of polyatomic molecules but may be harder to fully characterize due multidimensional nature of the problem.

## 1.2 Spectroscopy and Dynamics of Nitrogen Dioxide

Here we report on time-resolved measurements of Vacuum UltraViolet (VUV) excited state vibrational wavepacket dynamics in $NO_2$, driven by strong Fermi Resonance coupling. Additionally, nonadiabatic coupling between vibrational and electronic coordinates leads to state-dependent predissociation. We observed that, in this case, the nonadiabatic coupling is relatively weak and the zeroth-order vibrational dynamics appears to proceed in a manner exactly analogous to restricted IVR, but with the additional effect of nonadiabatic electronic (i.e. predissociation) coupling to directly dissociative configurations. In Fig. 1 we show a depiction of the TRPES scheme used here and the VUV-excited states and cation states of $NO_2$ relevant to this experiment. The left panel shows potentials as a function of bend angle $\alpha$ at NO bond lengths fixed to their equilibrium values. The right panel shows potentials as a function of one NO bond length, fixing the other NO bond and bend angle. In a TRPES experiment[33], an ultrafast pump pulse $\hbar\omega_{pump}$ prepares an excited state vibronic wavepacket. An ultrafast probe pulse $\hbar\omega_{probe}$ subsequently photoionized this vibronic wavepacket as a function of time delay $\Delta t$. The resulting photoelectron spectrum $S(\varepsilon)$ is measured as a function of kinetic energy, angle and time delay.

The $NO_2$ electronically excited state manifold spanned by the fs VUV (7.73 eV) pump pulse used here incorporates a number of repulsive valence states and predissociated Rydberg states[56,57]. In this energy region, the excited vibrational states in the 3p Rydberg are predissociative, meaning they are coupled to neutral continua (fragmentation channels). In this sense, the excited state levels should rather be thought of as compound scattering resonances with linewidths inversely related to their decay lifetimes. Some of these resonances likely couple to repulsive valence states via a$_1$ bending vibrational mode excitations[58]. As discussed below, the VUV-excited

wavepacket will be comprised of mixed zeroth-order valence and Rydberg electronic states, vibrational Fermi polyads (strong multi-mode vibrational mixing, *vide infra*) and mode-dependent predissociation dynamics. As will be shown, although triatomics constitute the simplest possible polyatomic molecule, such a wavepacket cannot be easily visualized as Gaussians propagating on an excited state potential energy surface, the picture associated with a molecular movie concept.

The $(1)^2A_1$ electronic ground state of $NO_2$ has the configuration $3a_1^2\ 2b_2^2\ 4a_1^2\ 5a_1^2\ 3b_2^2\ 1b_1^2\ 4b_2^2\ 1a_2^2\ 6a_1^1\ |\ 2b_1^0\ 7a_1^0\ 5b_2^0$. Ritchie and Walsh assigned the dominant single-photon electronic transition in the 7.7-9.1 eV spectral region to excitation to a zeroth-order $3p\sigma^2\Sigma_u$ Rydberg state[59]. This $n = 3$ Rydberg state converges to the linear electronic ground state of the $NO_2^+$ cation with an adiabatic Ionization Potential (IP) of $9.586 \pm 0.002$ eV[60]. Importantly, the VUV-excited state also contains zeroth-order $^2B_2$ valence electronic character, the likely source of oscillator strength, at the bent bond-elongated Franck-Condon geometry. As a relevant example, the $(3)^2B_2$ valence state is comprised of mixed $6a_1 \leftarrow 5a_1$ and $2b_1 \leftarrow 1a_2$ electronic character at the initially bent nuclear geometry[56]. Optical-optical double-resonance spectroscopy fixes a term energy of 6.899 eV at the relaxed, linear equilibrium geometry, associated with dominant Rydberg electronic character[61]. Above $\sim$7.5 eV, the $\sim$7.0-9.1 eV absorption band displays a perturbed vibrational progression in $v_1'$ and $v_2'$ with respective quanta of $\sim$1420 cm$^{-1}$ and $\sim$600 cm$^{-1}$ and an associated Fermi resonance that results in a $\sim$200 cm$^{-1}$ progression across the peak of the band (8.61 eV)[59,61]. At our 7.73 eV VUV excitation energy, the zeroth-order $3p\sigma^2\Sigma_u$ state exhibits vibrational structure containing strongly Fermi mixed quanta of symmetric stretch and/or bending mode excitations and is overlapped by an underlying, continuous electronic absorption band structure[59]. Other zeroth-order electronic states exist in this spectral region, including the Rydberg $3p\pi\ ^2\Pi_u$ state which also correlates with the ground $^1\Sigma^+$ state of the cation,[61], and two zeroth-order valence states - $(3)^2B_2$ and $(2)^2A_1$ - which correlate with the $NO(X)^2\Pi_\Omega + O(^1D_2)$ and $NO(X)^2\Pi_\Omega + O(^3P_J)$ neutral dissociation limits[56]. In addition, $3s\sigma$ and $3d\sigma$, $3d\pi$ and $3d\delta$ states exist in this VUV energy region. Following single-photon excitation at 7.87 eV (157.6 nm excimer laser), highly rovibrationally excited $NO(X)^2\Pi_\Omega$ photofragments were observed to be predominantly correlated with $O(^3P_J)$ atoms[62]. At similar two-photon excitation energies, $NO(X)^2\Pi_\Omega$ fragments were detected which correlated with both $O(^3P_J)$ and $O(^1D_2)$ atomic co-fragments[63]. Collectively, this implies that both the $(3)^2B_2$ and $(2)^2A_1$ valence excited states may be involved in the photofragmentation dynamics. This suggests that 3p Rydberg-valence mixing with these valence states, followed by direct valence dissociation, is one likely predissociation mechanism for the zeroth-order $3p\sigma^2\Sigma_u$ Rydberg state. Other mechanisms for predissociation of the $3p\sigma^2\Sigma_u$ state could conceivably involve vibrational coordinate dependent Rydberg-Rydberg couplings, as the other Rydberg states in this region support only dissociation continua. These vibrational mode dependent couplings would be manifested various ways, including as a coordinate dependence of the quantum defect[58].

We now consider the nature of the complex excited state vibronic wavepacket formed in $NO_2$. A fs VUV pump pulse ($\hbar\omega_{\text{pump}}$, purple) excites $NO_2$ from its $(1)^2A_1$ electronic ground state to the coupled $(3)^2B_2$ valence and $3p\sigma^2\Sigma_u$ Rydberg states. The initially prepared wavepacket, due to oscillator strengths and Franck-Condon overlap with the ground state, is dominated by zeroth-order $(3)^2B_2$ valence electronic character. The wavepacket then undergoes rapid electronic-nuclear evolution, developing increasingly $3p\sigma^2\Sigma_u$ Rydberg character as a function of time. It is also possible that some direct dissociation from the $(3)^2B_2$ component occurs in competition with the development of Rydberg character[56]. The complex polyad vibrational dynamics within the relatively long-lived 3p Rydberg state, and their coupling to predissociation continua, are the primary concerns of this paper. We emphasize that the zeroth-order 3p Rydberg aspect is the component of the excited state vibronic wavepacket most favourably projected onto the cation ground electronic state. Therefore, this specific (i.e. 400 nm probe pulse) TRPES experiment essentially 'projects' out the evolving 3p Rydberg character of the vibronic wavepacket, allowing us to monitor the complex vibrational polyad dynamics and decay in that zeroth-order state. In both panels, neutral valence predissociation pathways are shown as black arrows, yielding neutral channel atomic and molecular fragments.

The formation of polyads (strong Fermi resonance mixing) in the relatively long-lived $3p\sigma^2\Sigma_u$ vibrational manifold was previously studied in detail using double resonance spectroscopy[25,64]. The observation of resolved vibrational structure and, as we show here, relatively long-lived quantum beats in our TRPES data, suggest that the predissociation may be treated as a peturbative (weak) coupling. This amounts to ascribing a state-dependent linewidth to the zeroth-order $3p\sigma^2\Sigma_u$ vibrational polyad states. We can therefore apply the polyad model to the set of quasi-bound states coherently prepared by the fs VUV pump pulse. However, we emphasize that the states thus prepared are of vibronic character. In a very qualitative sense, the polyad nature of the vibrational states means that the "ion core" associated with the 3p Rydberg electronic component of the wavepacket is structurally very complex. It does not "look" anything like a point charge Coulomb potential and varies from polyad to polyad, leading to vibrational coordinate dependent quantum defects[65]. Furthermore, the change in the structure of the polyad vibrational wavefunction from one polyad to another (*vide infra*) means that the electronic wavefunction tacitly associated with each vibrational wavefunction must also vary from state to state. This variation of electronic structure with polyad vibrational state means that the coordinate dependence of the electronic part of the photoionization transition dipole matrix element cannot be accurately replaced by its expectation value: the Franck-Condon approximation likely does not hold rigorously here. It is important to note that the fs VUV pump pulse creates an vibronic wavepacket and, therefore, both vibrational dynamics and charge oscillations on the molecular frame occur in concert. This variation of electronic wavefunction with polyad state may be related to the strong (order of magnitude) mode-specificity previously seen, for higher Rydberg states of the same series, in autoionization rates[66] and, as we discuss below, potentially to trends in the neutral predissociation lifetimes seen here.

This paper is organized as follows. In Section II, the experimental setup, previously described in detail[67], is briefly described. In this experiment, a vibronic wavepacket containing zeroth-order $3p\sigma^2\Sigma_u$ Fermi vibrational polyad character is prepared by excitation with
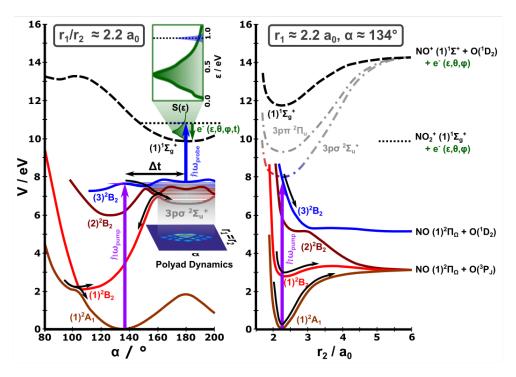
**Fig. 1** Potential energy curves of $NO_2$ relevant to the TRPES experiments. In the left panel, potentials are shown as a function of bend angle $\alpha$ at NO bond lengths $r_1 = r_2$ fixed to their equilibrium value of $\approx 2.2$ bohr. In the right panel, potentials are shown as a function of NO bond length $r_2$ at fixed $r_1$ and $\alpha$. A fs VUV pump pulse ($\hbar\omega_{pump}$, purple) excites $NO_2$ from its $(1)^2A_1$ electronic ground state to a region which includes the strongly coupled $(3)^2B_2$ valence and $3p\sigma^2\Sigma_u$ Rydberg states. The initially prepared wavepacket undergoes rapid electronic-nuclear evolution, developing increasing $3p\sigma^2\Sigma_u$ Rydberg character. The complex polyad vibrational dynamics within the $3p$ Rydberg state and its coupling to predissociation continua are the main foci of this investigation. A fs UV probe pulse ($\hbar\omega_{probe}$, blue) projects the evolving electronic-nuclear wavepacket, as a function of time, to energies above the ionization potential producing $NO_2^+$ $\left(X^1\Sigma_g^+\right) + e^-(\Delta t, \varepsilon, \theta, \phi)$. The kinetic energy and angular distributions of the emitted photoelectrons $S(\varepsilon)$ (green) are measured as a function of time delay $\Delta t$. The left panel exemplifies a path along which the dynamics proceed from initial excitation towards a linear geometry in the $3p\sigma^2\Sigma_u$ Rydberg state. It is in this 3p Rydberg configuration that the excited state wavepacket is most favourably projected onto the cation ground state electronic continuum. This allowed us to monitor the complex vibrational polyad dynamics. In both panels, the coupling to neutral predissociation pathways (black arrows), likely via bent configurations, produces neutral atomic and molecular fragments as shown.

a 160.4 nm, 70 fs pulse. The subsequent dynamics are probed by TRPES using a 400 nm, 40 fs probe pulse. In Section III, the main experimental results are presented. In Section IV, we present some details of the relevant spectroscopic and theoretical background required to understand these results. In Section V, we offer an interpretation of our results, in particular an assignment of the quantum beat frequencies observed in the experiment, based on the spectroscopic Hamiltonian described in Section IV. Along with the an analysis of the TRPES spectrum, a qualitative picture of the excited state wavepacket dynamics is presented in this section. We will emphasize that (i) strong Fermi mixing precludes any simple normal mode pictures of vibrational wavepacket dynamics and (ii) that a correlated electronic wavepacket must be associated with the vibrational dynamics. The essential quantum mechanical description of VUV excited state wavepacket dynamics in $NO_2$ begets the title of the paper. In Section VI, we provide a summary and a discussion of directions for future research.

## 2 Experiment

The optical setup and Velocity Map Imaging (VMI) spectrometer used in these experiments have been described in detail elsewhere[67,68]. Briefly, the ultrafast laser system (Coherent Legend Elite Duo) employed throughout this experimental study delivered 7.5 mJ, 35 fs pulses at 1 kHz, with a central wavelength of 800 nm. A 3.25 mJ component of the total laser output was split to generate the pump and probe arms, respectively. For the probe arm, 750 $\mu$J was used to generate 400 nm approximately 40 fs pulses in a thin (150 $\mu$m) BBO crystal. This was attenuated to 20 $\mu$J per pulse for the experiments reported here. The fs pump pulses were derived from a 2.5 mJ pulse at 800 nm via fifth harmonic generation to produce 160.4 nm, $\approx 0.5$ $\mu$J VUV pulses using a non-collinear four-wave difference-frequency mixing scheme first demonstrated by Noack and coworkers[69,70]. The VUV pulses had a spectral bandwidth of 1.5 nm, consistent with a Fourier-limited pulse duration of 33 fs. Due to propagation through the harmonic-generating gas and the VMI chamber input window, this was broadened to approximately 77 fs inside the VMI spectrometer (vide infra). The relative time delay between the pump and probe pulses was varied by a motorized delay stage (Newport XML210) in the probe arm. Each pulse was loosely focused into the VMI spectrometer using curved spherical reflective mirrors of 1.5 m and 2 m focal lengths for the pump and probe beams, respectively. The

pump and probe beams were collinearly recombined on a thin dichroic mirror having high reflectivity at 160 nm and high transmission at 400 nm. In the interaction region of the spectrometer, the laser pulses then crossed a seeded pulsed ($\approx$20 $\mu$s) molecular beam (1.5% $NO_2$, 3% $O_2$, in He at a stagnation pressure of 25 psi) generated by gas expanded through a kHz Even-Lavie pulsed valve[71] and skimmed through a 1 mm diameter skimmer. The nozzle was maintained at $60^o$C in order to minimize the contribution of $N_2O_4$ in the beam. The small amount of $O_2$ in the beam helps purify the $NO_2$ (removing NO by back-reaction) but otherwise has no effect on the present experiment. The base pressure in the VMI spectrometer was $\approx 10^{-9}$ torr, with an order of magnitude increase upon introduction of the pulsed molecular beam. In vacuo sets of blackened conical light baffles along the laser axis were used to significantly reduce scattered light due to the VUV laser. Photoelectrons generated in the interaction region via molecular ionization were accelerated by the VMI lens into a chevron stack micro-channel plate (MCP) detector coupled to a phosphor screen. A Thorlabs DC210 CCD camera was used to collect images from the phosphor screen.

For calibration, we measured the TRPES for $1 + 2'$ ionization of Xe (5% in Helium at 27 psi) with the pump and probe spatially and temporally overlapped in the VMI spectrometer. Two peaks corresponding to the spin-orbit split $J = 1/2$ and $J = 3/2$ components of the ground electronic state of $Xe^+$ were observed. The splitting between these peaks was used as an energy calibration for the spectrometer, the resolution being 320 meV under these conditions. A pump-probe delay scan of the integrated yield of the $J = 1/2$ peak provided an *in-situ* cross-correlation, determining the time resolution of the experiment. Fitting yielded a Gaussian full-width-at-half-maximum (FWHM) of 82$\pm$10 fs. For a 40$\pm$3 fs FWHM probe pulse, this then determined a 77$\pm$12 fs FWHM duration for the 160.4 nm pump pulse, the broadening being a result of propagation which includes dispersion due to the 0.5 mm thick $CaF_2$ entrance window to the VMI spectrometer.

Wavepacket dynamics of $NO_2$ resonantly excited by the VUV pump pulse were studied by TRPES. Photoelectrons were generated by single probe photon ionization of the excited state and their kinetic energy and angular distributions were measured as a function of pump-probe time delay. 100, 30 ms exposure images were collected at each time delay, with and without the molecular beam. The 'no-beam' background was dynamically subtracted in order to remove any delay dependent signal from background molecules in the spectrometer, as well as residual background photoelectrons produced by scattered 160 nm photons hitting metal surfaces inside the spectrometer. The data were recorded between time delays of -500 fs and 2 ps with respect to the cross correlation peak, and with a temporal step size of 20 fs. The centroid of the Xe cross correlation determined the time zero, $t_0$, for the pump-probe delay scans. The TRPES described below resulted from the average of 20 such delay scans. Standard inverse Abel transform processing was applied to convert the recorded photoelectron images into kinetic energy and angular distributions. The time-resolved photoelectron angular distributions were also collected. In some cases, the time-resolved photoelectron anisotropy parameters reflect complimentary aspects of the excited state wavepacket dynamics [72–74]. In the present case, however, the extracted anisotropy parameters revealed the same quantum beats as seen in the kinetic energy distributions. These are not discussed further, as they do not provide any additional information in this case.

## 3    Results

In Fig. 2(a) we show the TRPES for $NO_2$ resonantly excited at 160.4 nm. Both decay and periodic oscillations are observed across the entire spectrum. In Fig. 2(b) we show the PES at 100 fs delay, where the maximum integrated photoelectron yield is observed. The symmetric stretch progression in the ionic ground state is barely resolved. The anticipated positions of the well known peaks in this progression[75] are marked by dashed red lines. Labeling the vibrational states in the conventional manner as $(v_1, v_2^l, v_3)$ – where $v_1$ is the number of quanta in symmetric stretch, $v_2^l$ in the bend with angular momentum $l$ and $v_3$ in the asymmetric stretch, the photoelectron spectrum maximizes at (5,0,0), and has significant intensity in the (3,0,0)-(7,0,0) range. The normalized, integrated yield over the observed symmetric stretch peaks is shown in Fig. 2(c). It can be seen that the (7,0,0) yield is observed to both rise and decay more rapidly and show a deeper modulation as a function of time delay than do the other vibrational peaks. In order to extract the oscillating components from the data, we follow the procedure described in[76]. A 2D global fit, excluding the oscillatory components, is performed using the equation,

$$S(E,t) = \exp\left(-[(t-t_0)/\tau]\right) \otimes \begin{cases} A_1(E)\exp(-t/\tau_1) + A_2(E)\exp(-t/\tau_2) + A_3(E)\exp(-t/\tau_3) \text{ if } t > t_0 \\ 0 \text{ if } t < t_0 \end{cases}$$

where $S(E,t)$ represents the measured TRPES. The kinetic decay time constants $\tau_1, \tau_2$, and $\tau_3$, and their corresponding energy resolved Decay Associated Spectra (DAS) $A_1(E)$, $A_2(E)$ and $A_3(E)$ are determined by non-linear 2D global fitting using the Levenberg-Marquardt algorithm. In Fig. 3(a) we reproduce the experimental TRPES data: the resulting 2D global fit to the data is shown in Fig. 3(b). It can be seen that the global fit generally describes well the decay kinetics of the TRPES data. The first extracted time constant is cross correlation limited, meaning $\tau_1 \leq 80$ fs. For the purposes of global fitting, we have used $\tau_1 = 77$ fs. The other two extracted time constants are $\tau_2$=0.45$\pm$0.05 ps and $\tau_3$=5.4$\pm$0.7 ps.

In Fig. 4 we present the DAS $A_1(E)$, $A_2(E)$ and $A_3(E)$ extracted from the 2D global fit. The first DAS $A_1(E)$ (black) associated with the fastest time constant maximizes towards zero electron kinetic energy, displays signals out to electron kinetic energies of $\sim$2.0 eV,
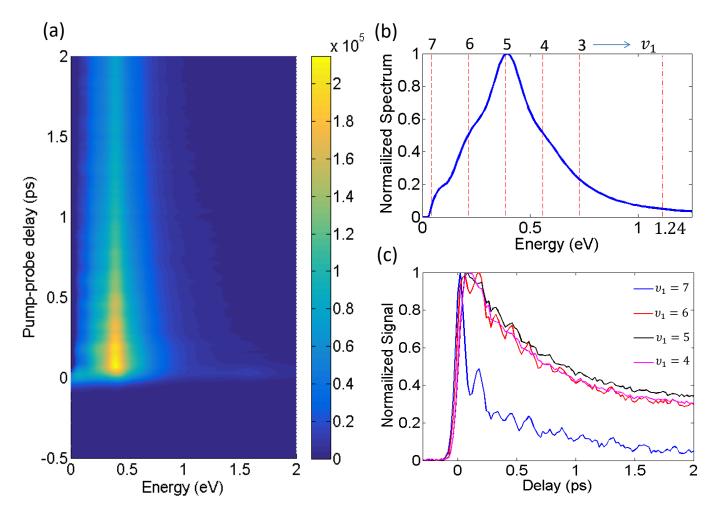
**Fig. 2** (a) TRPES of $NO_2$ for 160.4 nm pump and 400 nm probe. The colour scale represents the photoelectron yield in arbitrary units. (b) The PES at a delay of 100 fs showing a barely resolvable $v_1$=3-7 progression in the symmetric stretch mode of the cation. (c) Time dependence of the photoelectron yields for different symmetric stretch final states of the cation. It can be seen that the decay and oscillation vary significantly with cation final vibrational state.
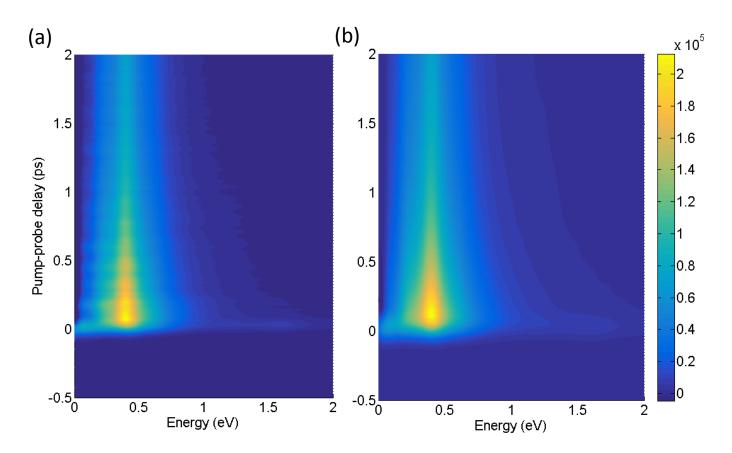
(a)



(b)



**Fig. 3** (a) TRPES of $NO_2$ for 160.4 nm pump and 400 nm probe, with the photoelectron signal amplitude being in arbitrary units. (b) A 2D global fit to the TRPES data using Eq. 3. The fit can be seen to accurately describe the decaying components in the TRPES data, allowing for extraction of three statistically significant kinetic time constants and their Decay Associated Spectra. For details, see the text.

and, interestingly, has negative values between 0.4-0.5 eV. The minor positive peak in the first DAS, appearing at an electron kinetic energy of ~1.6 eV, indicates that a (1+2') ionization mechanism is active at early pump-probe delay times. Considering this, the major (<0.4 eV) and minor (~1.6 eV) positive peaks in the DAS $A_1(E)$ are fully consistent with initial excitation to the $(3)^2B_2$ valence state (with predominant $6a_1 \leftarrow 5a_1$ and $2b_1 \leftarrow 1a_2$ electronic characters with respect to the electronic ground state configuration[56]) at the initially bent nuclear geometry. At early times, this configuration seems to be readily ionized to the Koopmans-correlated[33] $(1)^3A_2$ cation state (i.e. $6a_1$ electron removal from $(3)^2B_2$ therefore leaves a 'hole' in the $5a_1$ orbital, corresponding to the $(1)^3A_2$ cation state) in its bent, quasi-bound configuration[77]. With its associated term energy of 13.593 eV[75] and pump and probe pulse bandwidths, this results in production of up to 0.4 eV kinetic energy electrons, as seen in the data. As the excited state wavepacket evolves, the bending angle and N-O bond lengths increase, the unbound region of the same $(1)^3A_2$ cation state and the first dissociative ionization limit of $NO_2$ becomes accessible at 12.380 eV[78,79], resulting in electron kinetic energies extending to ~1.7 eV.

Concerning the negative values, these are only possible in a DAS for a sequential (A → B → ...) kinetic mechanism[76]. This, combined with the cross-correlation limited time dependence of $A_1(E)$, suggests that the configuration initially prepared by the fs VUV pump pulse has a broad photoelectron spectrum maximizing towards zero electron kinetic energy (indicating a significant geometry change with respect to the cation ground electronic state) and that this rapidly ($\tau_1 = 77$ fs) decays to a new configuration having a photoelectron spectrum $A_2(E)$ (red) with a relatively sharp maximum in the 0.4-0.5 eV range, suggestive of a much smaller geometry change with respect to the cation ground state. Interestingly, the 0.4-0.5 eV energy region is associated with both $\tau_2$ and $\tau_3$, with very little change in their respective DAS. There are no negative components seen in $A_2(E)$, indicating that it cannot be assigned to be a sequential kinetic intermediate existing transiently between the initial (which decays with $\tau_1$) and third (which would decay with $\tau_3$) configurations. This then leaves the kinetic possibility that the intermediate configuration decays via a parallel mechanism (i.e. simultaneously $\tau_2$ and $\tau_3$) to an undetected channel. However, this is only kinetically possible if the rapid decay of the initial configuration simultaneously prepares two energetically overlapping but 'independent' configurations having nearly identical DAS, namely $A_2(E)$ (red) and $A_3(E)$ (blue). Each 'independent' intermediate configuration must then decay with its own time constant ($\tau_2$ or $\tau_3$, respectively) to an undetected channel. A possible interpretation of a parallel decay mechanism for the second kinetic step suggested by the 2D global fits will be discussed in a following section.
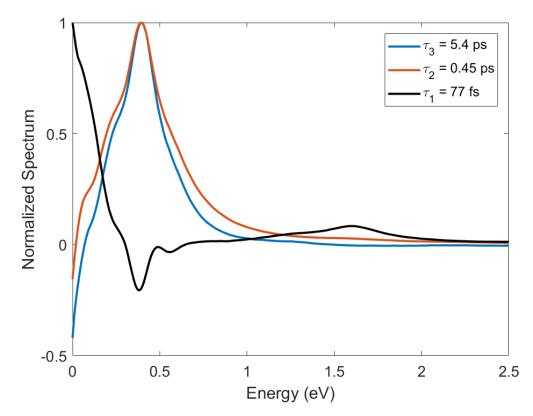
**Fig. 4** The 2D global fit to the TRPES data, shown in Fig. 3(b), permitted the fitting of three Decay Associated Spectra $A_1(E)$ (black), $A_2(E)$ (red) and $A_3(E)$ (blue) associated with the decay constants $\tau_1 = 77$ fs, $\tau_2 = 0.45$ ps and $\tau_3 = 5.4$ ps, respectively. For a discussion of kinetic mechanisms consistent with these spectra and time constants, see the text.

The 2D global fits were subtracted from the TRPES data, yielding the fit residuals shown in Fig. 5(a). It can be seen that the residuals exhibit periodic oscillations. The Fourier transform power spectrum of these residuals is shown in Fig. 5(b). The peak centered at $236\pm8$ cm$^{-1}$, extending from 202 cm$^{-1}$ to 253 cm$^{-1}$, pervades the entire spectrum and represents the $\approx145$ fs oscillation seen clearly in the time delay scans. This is consistent with the dominant energy spacing observed in the NO$_2$ absorption spectrum in the 7.7 - 9.2 eV range[59,80]. Two lower frequency peaks are also observed: one centered at $151 \pm5$ cm$^{-1}$, extending from 134 cm$^{-1}$ to 168 cm$^{-1}$; and one centered at $84 \pm5$ cm$^{-1}$ extending from 67 cm$^{-1}$ to 101 cm$^{-1}$. Additionally, it can be seen that the 151 cm$^{-1}$ oscillation has a stronger contribution at lower photoelectron energies, between 0 and 0.2 eV, whereas the 84 cm$^{-1}$ oscillation appears at slightly higher energies between 0.11 and 0.38 eV. At still higher photoelectron energies, this latter peak also has a shoulder at $33 \pm1$ cm$^{-1}$. The low frequency peak around 17 cm$^{-1}$ is in the region corresponding to the inverse duration of the temporal scan range (2 ps) and therefore cannot be reliably analyzed.

## 4 Theoretical Model

### 4.1 Pump Transition: Quasi-Bound States

As discussed in the Introduction, electronic states of the NO$_2$ $n =3$ Rydberg manifold lie within the bandwidth[59] of the fs VUV pump pulse. The oscillator strength for this pump transition likely derives (i.e. intensity borrowing) from the initially phased zeroth-order $^2B_2$ valence character in the vibronic wavepacket. This, based on our kinetic models, rapidly dephases, yielding zeroth-order $3p\sigma^2\Sigma_u$ Rydberg character which in turn is apparently relatively long lived. The zeroth order $3p\sigma^2\Sigma_u$ Rydberg vibrational eigenstates are characterized by coupling to an underlying close-coupled continuum[56], meaning that these states are predissociative and may formally be thought of as narrow line width scattering resonances in the excited state. The $3p\sigma^2\Sigma_u$ state has been the subject of previous rotationally resolved optical-optical double-resonance spectroscopic studies[64]. Bend and symmetric stretch normal mode states in this manifold couple strongly via Fermi resonance resulting in a approximately 220 cm$^{-1}$ spacing which pervades the absorption spectrum[59]. A 33 cm$^{-1}$ splitting is also observed in the spectrum[59], and assigned to transitions occurring from different initial rotational states. Since these represent incoherently populated states, this particular 'hot band' splitting in the absorption spectrum cannot explain the 33 cm$^{-1}$ quantum beat observed in our TRPES data. The Fermi Resonance coupling is linear in the stretching coordinate and quadratic in the bending coordinate. This results in blocks of states, or polyads, which can be built from normal mode basis states: the normal mode picture simply does not apply in the $3p\sigma^2\Sigma_u$ state of NO$_2$. The resultant vibronic states can therefore be described as polyad vibrational
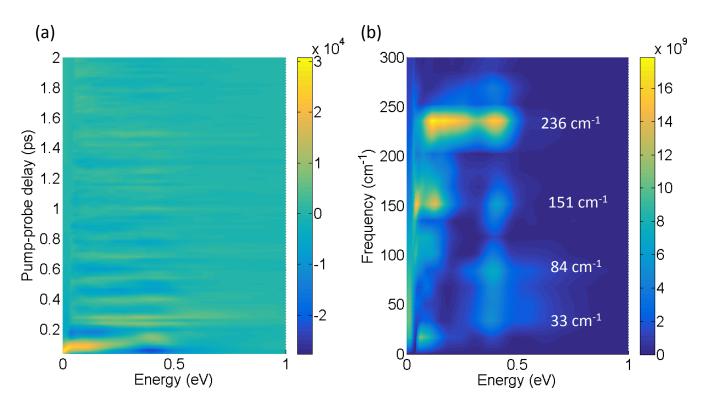
**Fig. 5** (a) The global fit residuals (TRPES data minus fit) reveal the purely oscillating components in the TRPES data. (b) Fourier transform power spectra of the fit residuals from (a). It can be seen that there are several dominant frequencies in these data. For a discussion, see the text.

states of zeroth-order $3p\sigma^2\Sigma_u$ Rydberg electronic character. The polyad vibrational states, as the nuclear states of a zeroth-order Rydberg state, do not couple to predissociation. However, each electronic component of the polyad states has amplitude in the region of short radial distances of the Rydberg electron where there are multi-electron configuration interactions.

In a vibronic wavepacket picture, there is some mixing of zeroth-order electronic states upon vibration, leading to Rydberg-Rydberg and Rydberg-valence coupling. Any crossings to other zeroth-order electronic states in this region leads to barrierless dissociation to separated neutral atomic and molecular fragments. There are in principle seven energetically open product channels (ignoring the lambda-doubling and spin-orbit splitting of the asymptotes)[56]. However, single photon photodissociation experiments at 157.6 nm revealed that the $NO(^2\Pi)+O(^3P)$ channel is dominant in this spectral region[62]. The weak coupling to the dissociative continuum ascribes a line width to each polyad member state which depends on its degree of coupling. The latter may be related to matrix elements of the spatial derivative of the quantum defect along a particular vibrational coordinate. A $3p\sigma^2\Sigma_u$ wavepacket thus prepared will simultaneously exhibit both multi-level quantum beats (indicating vibrational energy flow) and population decay (indicating mode specific predissociation). This situation can therefore be considered to be the polyatomic analogue of the predissociative wavepacket dynamics previously seen in the diatomic IBr[55]. Unfortunately, the complex Rydberg-valence mixing and their coupling to neutral continuum (predissociation) channels is not presently well understood. However, given our observation of persistent quantum beats, we will assume that the coupling to the dissociative continuum can be approximated as a weak perturbation, thus assigning state-dependent line widths to each of the states within the Fermi-mixed polyads.

Fermi resonance mixing in the $3p\sigma^2\Sigma_u$ vibrational manifold is well characterized[25,64]. This allows us, therefore, to apply the Fermi resonance model to generate the sub-set of quasi-bound states coherently prepared by the fs VUV pump pulse. We remind that the Fermi resonance is linear in the symmetric stretch and quadratic in the bend: for example, in ground state $CO_2$ the stretch:bend frequency ratio is 1:2. The span of coupled zeroth-order normal mode basis states must reflect this ratio (i.e. from (n,0,0) to (0,2n,0) ). We now introduce our nomenclature for the polyads. As an illustrative example, the normal mode basis state (5,0,0) contributes to the polyad {(5,0,0),(4,2,0),(3,4,0),(2,6,0),(1,8,0),(0,10,0)}. Henceforth we will label each polyad by its span of normal mode basis states, identifying the largest symmetric stretching and bending quanta, respectively. For instance, the above example will be referred to as the (5,0,0)-(0,10,0) polyad. We further label eigenstates within each polyad as $\gamma = 1, 2..$ in order of increasing energy. Normal mode basis

states in such a polyad are strongly mixed by the interaction Hamiltonian describing Fermi resonance[25,64],

$$V_{ij} = \left\langle v_1, v_2^l, v_3 \left| H_{int} \right| v_1 - 1, v_2^l + 2, v_3 \right\rangle$$

$$= \frac{-k_{122}}{2\sqrt{2}} \sqrt{[(v_2 + 2)^2 - l^2]v_1}, \tag{1}$$

where $V_{ij}$ are the matrix elements of the interaction Hamiltonian, $i$ and $j$ being indices corresponding to vibrational quantum numbers. Matsui $et\ al$[64] determined, from their rotationally resolved double-resonance spectra, the coupling constant $k_{122}$ to be -74.56 cm$^{-1}$. We will ignore here higher order ($6^{th}$ order and above) mixing terms. The energies of polyad vibrational levels in the $3p\sigma^2\Sigma_u$ state can then be computed by diagonalizing the full Hamiltonian matrix, which includes the interaction. It can be rewritten as,

$$H_{ij} = E_0 \delta_{ij} + V_{ij} \tag{2}$$

where,

$$E_0 = \omega_1 \left( v_1 + \frac{1}{2} \right) + \omega_2 (v_2 + 1) + \omega_3 \left( v_3 + \frac{1}{2} \right)$$

$$+ \chi_{11} \left( v_1 + \frac{1}{2} \right)^2 + \chi_{22} \left( v_2 + \frac{1}{2} \right)^2 + \chi_{33} \left( v_3 + \frac{1}{2} \right)^2$$

$$+ g_{22}l^2 + \chi_{21} \left( v_1 + \frac{1}{2} \right)(v_2 + 1) \tag{3}$$

$$+ \chi_{32}(v_2 + 1)\left( v_3 + \frac{1}{2} \right).$$

The harmonic mode frequencies $\omega_1$, $\omega_2$ and $\omega_3$, and the associated anharmonic constants were previously determined[64].

In the following, in order to obtain the dipole selection rules, we will treat the transitions from the ground state as if they are directly to the 3p Rydberg manifold. To determine the composition of the excited state wavepacket, we must also consider the angular momenta of the involved 3p Rydberg rovibronic states. The excited state 3p vibronic levels are additionally labeled by the projection quantum number $\Lambda$ of the angular momentum onto the symmetry axis (i.e. the bond axis for linear molecules) as $\Sigma_{g/u}$ for $\Lambda=0$, $\Pi_{g/u}$ for $\Lambda=1$, $\Delta_{g/u}$ for $\Lambda=2$ etc.[64,81]. We must additionally consider the inversion and permutation symmetry of the eigenstates within the $3p\sigma^2\Sigma_u$ manifold. Since NO$_2$ has a linear geometry in the 3p state (as does the cation ground state and all correlated Rydberg states), the rovibronic levels are labeled by irreducible representations of $D_{\infty h}(M)$ as being symmetric/anti-symmetric ($+/-$) under inversion. In addition, due to the Pauli Exclusion Principle, eigenstates are necessarily symmetric ( s ) with respect to permutation of the (bosonic) spin zero $^{16}$O atoms. Since only ($+$, s) or ($-$, s) states are allowed, $\Sigma_{g/u}$ vibronic levels permit only states of even angular momentum $N$ (total angular momentum less the spin). Larger projection angular momenta ($\Pi_{g/u}, \Delta_{g/u}$) will permit all states with $N$ greater than or equal to the projection angular momentum: for instance $\Pi_{g/u}$ states can only have $N \geq 1$. The ground state of the molecule is subject to the same labels and constraints, except that the projection angular momentum can be approximated by the symmetric top quantum number $K$. Symmetry selection rules permit only $+ \leftrightarrow -$, $\Delta J = 0, \pm 1$ for single photon dipole allowed transitions. Examples of allowed transitions originating from the ground state into the (5,0,0)-(0,10,0) $\Sigma_u$ and (5,1$^1$,0)-(0,11$^1$,0) $\Pi_g$,(4,1$^1$,0)-(0,9$^1$,0) $\Pi_g$ polyad states are shown in Fig. 6. Table 1 lists the energies of the states accessible by our fs VUV pump pulse. These energies are eigenvalues of the Hamiltonian in Eq. 2.

Although not accurate due to Rydberg-valence coupling, we will nevertheless assume here that population of each 3p polyad state is approximately proportional to its Franck-Condon (FC) overlap $\langle v_g | p\gamma \rangle$ with the vibrational ground state $|v_g\rangle$, where $\gamma$ denotes a particular eigenstate within the polyad $p$. The $|p\gamma\rangle$ are obtained in the normal mode basis by diagonalization of Eq. 2. In Table 1 we present the coefficients in the normal mode basis set expansion for the four polyads spanned by the fs VUV pump pulse. It can be seen that the states prepared by the pump pulse are highly mixed. On the left column of Table 1, we introduce a short hand notation: for example, $|\Sigma_u\gamma\rangle$ for the (5,0,0)-(0,10,0) $\Sigma_u$ polyad (the third block), and $|\Delta_u\gamma\rangle$ for the (4,2$^2$,0)-(0,10,0) $\Sigma_u$ polyad (the second block). Continuing with this notation, we use $|X\Pi_g\gamma\rangle$ for the (4,1$^1$,0)-(0,9$^1$,0) $\Pi_g$ polyad (top block), and $|A\Pi_g\gamma\rangle$ for the (5,1$^1$,0)-(0,11$^1$,0) $\Pi_g$ polyad (bottom block). The strong Fermi resonances thoroughly invalidate any simple bend-stretch interpretation of the eigenstates. The (bent) ground state vibrational wavefunction $|v_g\rangle$ is approximated as a direct product of Gaussian functions of the excited state normal coordinates. The symmetric stretch and degenerate bend Gaussian functions are centered at a displacement equal to the ground state bond length and bend angle respectively, and their widths are taken as the harmonic widths corresponding to the ground state bend and stretch frequencies. The FC factors $|\langle v_g | p\gamma \rangle|^2$ are given in the second from right column in Table 1. It is evident that some eigenstates within the polyad blocks have FC factors orders of magnitude larger than all others: these are indicated in **bold**. The excitation probability of the states will be determined by both their energetic overlap with the (Gaussian) envelope of the fs VUV pump pulse spectrum, and their approximate FC overlap with the ground state. The excitation amplitude to first order in perturbation theory
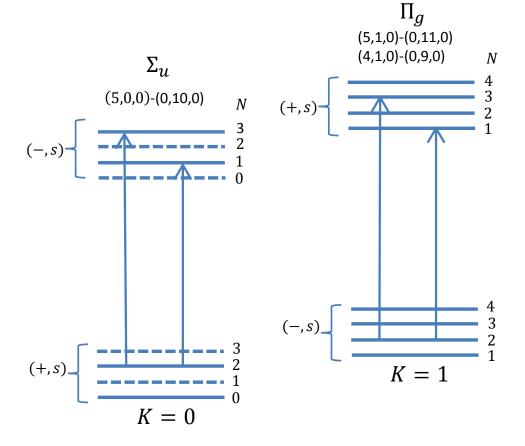
**Fig. 6** Rotational selection rules for pump transitions into the $3p\sigma^2\Sigma_u$ state of $NO_2$. Shown are examples of $P$ and $R$-branch, symmetry allowed, single photon dipole transitions originating from the $K = 0$ and $K = 1$ rotational stacks in the ground state. The states are labelled by the angular momentum quantum number $N$ (total angular momentum less the spin). The (non-existing) rotational states forbidden by the Pauli principle are shown as dashed lines.

| $\lvert p\gamma\rangle$ | Normal Mode Expansion | approx. FC Factors | $E_{p\gamma}(\text{cm}^{-1})$ |
|---|---|---|---|
| $\lvert X\Pi_g 1\rangle$ | $0.1632\lvert 41^10\rangle$-$0.4287\lvert 33^10\rangle$+$0.6315\lvert 25^10\rangle$-$0.5607\lvert 17^10\rangle$+$0.2764\lvert 09^10\rangle$ | **1.2e-3** | **61,000** |
| $\lvert X\Pi_g 2\rangle$ | $-0.4103\lvert 41^10\rangle$+$0.5850\lvert 33^10\rangle$-$0.1348\lvert 25^10\rangle$-$0.4739\lvert 17^10\rangle$+$0.4966\lvert 09^10\rangle$ | 1.7e-5 | 61,310 |
| $\lvert X\Pi_g 3\rangle$ | $-0.5961\lvert 41^10\rangle$+$0.1784\lvert 33^10\rangle$+$0.5075\lvert 25^10\rangle$-$0.0317\lvert 17^10\rangle$-$0.5952\lvert 09^10\rangle$ | 6.4e-7 | 61,601 |
| $\lvert X\Pi_g 4\rangle$ | $0.5840\lvert 41^10\rangle$+$0.4239\lvert 33^10\rangle$-$0.0725\lvert 25^10\rangle$-$0.4794\lvert 17^10\rangle$-$0.4941\lvert 09^10\rangle$ | 1.4e-7 | 61,866 |
| $\lvert X\Pi_g 5\rangle$ | $-0.3296\lvert 41^10\rangle$-$0.5122\lvert 33^10\rangle$-$0.5658\lvert 25^10\rangle$-$0.4789\lvert 17^10\rangle$-$0.2804\lvert 09^10\rangle$ | 1.5e-8 | 62,080 |
| $\lvert \Delta_u 1\rangle$ | $0.2180\lvert 42^20\rangle$-$0.4925\lvert 34^20\rangle$+$0.6358\lvert 26^20\rangle$-$0.5046\lvert 18^20\rangle$+$0.2259\lvert 010^20\rangle$ | 2.7e-5 | 61,605 |
| $\lvert \Delta_u 2\rangle$ | $-0.4726\lvert 42^20\rangle$+$0.5430\lvert 34^20\rangle$+$0.0034\lvert 26^20\rangle$-$0.5279\lvert 18^20\rangle$+$0.4507\lvert 010^20\rangle$ | 9.9e-6 | 61,936 |
| $\lvert \Delta_u 3\rangle$ | $-0.6067\lvert 42^20\rangle$+$0.0435\lvert 34^20\rangle$+$0.5195\lvert 26^20\rangle$+$0.0840\lvert 18^20\rangle$-$0.5942\lvert 010^20\rangle$ | 2.2e-6 | 62,258 |
| $\lvert \Delta_u 4\rangle$ | $-0.5374\lvert 42^20\rangle$-$0.4929\lvert 34^20\rangle$-$0.0471\lvert 26^20\rangle$+$0.4278\lvert 18^20\rangle$+$0.5319\lvert 010^20\rangle$ | 4.5e-7 | 62,552 |
| $\lvert \Delta_u 5\rangle$ | $-0.2688\lvert 42^20\rangle$-$0.4666\lvert 34^20\rangle$-$0.5689\lvert 26^20\rangle$-$0.5259\lvert 18^20\rangle$-$0.3314\lvert 010^20\rangle$ | 5.4e-8 | 62,797 |
| $\lvert \Sigma_u 1\rangle$ | $0.0716\lvert 500\rangle$-$0.2553\lvert 420\rangle$+$0.5075\lvert 340\rangle$-$0.6258\lvert 260\rangle$+$0.4846\lvert 180\rangle$-$0.2136\lvert 0100\rangle$ | **1.5e-2** | **61,591** |
| $\lvert \Sigma_u 2\rangle$ | $-0.2386\lvert 500\rangle$+$0.5340\lvert 420\rangle$-$0.4667\lvert 340\rangle$-$0.0838\lvert 260\rangle$+$0.5184\lvert 180\rangle$-$0.45054\lvert 0100\rangle$ | **1.3e-3** | **61,904** |
| $\lvert \Sigma_u 3\rangle$ | $-0.4690\lvert 500\rangle$+$0.4891\lvert 420\rangle$+$0.1953\lvert 340\rangle$-$0.4313\lvert 260\rangle$-$0.2032\lvert 180\rangle$+$0.5248\lvert 0100\rangle$ | 2.8e-5 | 62,186 |
| $\lvert \Sigma_u 4\rangle$ | $0.6150\lvert 500\rangle$+$0.0209\lvert 420\rangle$-$0.4482\lvert 340\rangle$-$0.3120\lvert 260\rangle$+$0.2181\lvert 180\rangle$+$0.5249\lvert 0100\rangle$ | 1.0e-6 | 62,440 |
| $\lvert \Sigma_u 5\rangle$ | $-0.5393\lvert 500\rangle$-$0.5162\lvert 420\rangle$-$0.2047\lvert 340\rangle$+$0.1909\lvert 260\rangle$+$0.4473\lvert 180\rangle$+$0.40553\lvert 0100\rangle$ | 7.8e-9 | 62,657 |
| $\lvert \Sigma_u 6\rangle$ | $0.2212\lvert 500\rangle$+$0.3788\lvert 420\rangle$+$0.4937\lvert 340\rangle$+$0.5306\lvert 260\rangle$+$0.4556\lvert 180\rangle$+$0.2734\lvert 0100\rangle$ | 1.6e-10 | 62,835 |
| $\lvert A\Pi_g 1\rangle$ | $-0.1154\lvert 51^10\rangle$+$0.3324\lvert 43^10\rangle$-$0.5585\lvert 35^10\rangle$+$0.6020\lvert 27^10\rangle$-$0.4170\lvert 19^10\rangle$+$0.1672\lvert 011^10\rangle$ | **1.2e-3** | **62,187** |
| $\lvert A\Pi_g 2\rangle$ | $0.3250\lvert 51^10\rangle$-$0.5671\lvert 43^10\rangle$+$0.3433\lvert 35^10\rangle$+$0.2298\lvert 27^10\rangle$-$0.5314\lvert 19^10\rangle$+$0.3460\lvert 011^10\rangle$ | 1.9e-5 | 62,514 |
| $\lvert A\Pi_g 3\rangle$ | $-0.5323\lvert 51^10\rangle$+$0.3636\lvert 43^10\rangle$+$0.3412\lvert 35^10\rangle$-$0.3448\lvert 27^10\rangle$-$0.3179\lvert 19^10\rangle$+$0.4981\lvert 011^10\rangle$ | 3.7e-7 | 62,821 |
| $\lvert A\Pi_g 4\rangle$ | $-0.5981\lvert 51^10\rangle$-$0.1863\lvert 43^10\rangle$+$0.3671\lvert 35^10\rangle$+$0.4038\lvert 27^10\rangle$-$0.1105\lvert 19^10\rangle$-$0.5455\lvert 011^10\rangle$ | 1.1e-7 | 63,108 |
| $\lvert A\Pi_g 5\rangle$ | $-0.4600\lvert 51^10\rangle$-$0.5434\lvert 43^10\rangle$-$0.3183\lvert 35^10\rangle$+$0.0847\lvert 27^10\rangle$+$0.4242\lvert 19^10\rangle$+$0.4524\lvert 011^10\rangle$ | 1.5e-8 | 63,359 |
| $\lvert A\Pi_g 6\rangle$ | $0.1687\lvert 51^10\rangle$+$0.3251\lvert 43^10\rangle$+$0.4666\lvert 35^10\rangle$+$0.5435\lvert 27^10\rangle$+$0.5006\lvert 19^10\rangle$+$0.3191\lvert 011^10\rangle$ | 1.3e-9 | 63,575 |

**Table 1** Normal mode expansions for 3p vibrational eigenstates within the four blocks of polyads, presented in energetic order. The approximate Franck-Condon Factors and eigenstate energies, for states lying within the bandwidth of the fs VUV pump pulse, are shown in the columns to the right of the table. It can be seen that some Franck-Condon factors are orders of magnitude larger than all others: these are indicated in **bold**. The short hand notational label $\lvert p\gamma\rangle$ (left) is described in the text.

is given by,

$$c_{p\gamma}(t_f) = -i/\hbar \int_{-\infty}^{t_f} e^{-2\ln 2[(t'-t_0)/\tau]^2 + i\omega_{p\gamma}t'} \cos(\omega_0 t')dt' \qquad (4)$$

within a normalization constant consisting of the laser electric field strength and the electronic dipole matrix element. $\tau$ is the transform limited FWHM duration of the pump pulse and $\omega_0$ is its center frequency, corresponding here to a photon energy of 62,350 cm$^{-1}$. $\omega_{p\gamma}$ is the angular frequency corresponding to the difference between the exact pump photon energy and the transition energy from the ground state to the state $\lvert p\gamma\rangle$. In Fig 7 we show the populations $\lvert c_{p\gamma}(t_f)\langle v_g \lvert p\gamma\rangle\rvert^2$ and energies of the polyad states which can be excited coherently out of the same initial ground rotational state, with linear and log Y- axis scales. These states, each having a different line width (not shown) determined by its predissociative coupling to the NO+O photofragment continuum, comprise the wavepacket which is probed as a function of time delay by the fs 400 nm photoionization probe laser pulse. In Fig. 8 we show the probability densities for the most populated eigenstates from each of the four polyads. These are plotted as a function of the excited state symmetry coordinates $S_1$ and $S_2$, which are proportional to the symmetric stretch and bend normal coordinates, respectively. The delocalization of the density and complex nodal structure along both coordinates is a result of the strong mixing evinced by Table 1. Importantly, the notion of 'structural dynamics' being represented by the 'trajectory' of a classically localized Gaussian wavepacket moving on an excited state potential surface fails completely here. Vibrational energy flow and predissociation in the $3p\sigma^2\Sigma_u$ state of NO$_2$ is fully quantum mechanical.

## 4.2 Probe Transitions : The Molecular Ionization Continuum

In TRPES, the time-delayed fs probe pulse projects the evolving set of coherently prepared excited intermediate states, such as described in the previous section, onto the molecular ionization continuum which acts as the final state or 'template' onto which the wavepacket dynamics are projected. The final state in the molecular photoionization continuum is often approximated as the direct product of the ionic core quantum state with that of a free scattered photoelectron. In this 'flat continuum' picture, the transition probabilities are dominated by the quantum states of the cation, with the free photoelectron acting as a 'spectator' required to conserve energy and angular momentum. This in turn leads to the considerable simplification that probe transition probabilities to final cation quantum states are governed by electronic (Koopmans' correlations) and vibrational (Franck-Condon factors) overlaps. This is termed direct ionization: all cation quantum states below the total (1+1') pump plus probe photon energy are energetically accessible and populated according to their overlaps with the excited state wavepacket. Via energy conservation, the kinetic energy of the free electron gives these final cation state populations at the end of the pump-probe sequence. Notably, Koopmans-correlated cation states also appear to
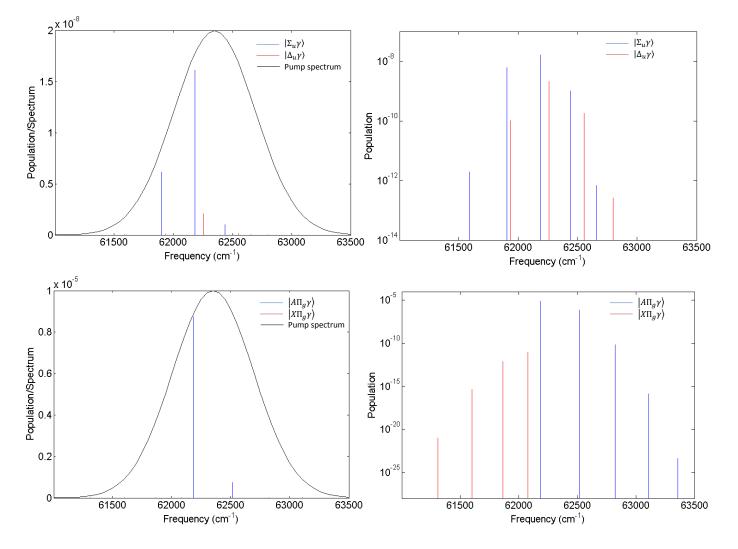
**Fig. 7** The energies of the eigenstates and the Franck-Condon factors determine the composition of the excited state wavepacket. Using linear (left) and semilog (right) scales, we show the excited state polyad populations. In the top row, we show the excited eigenstates states coherently prepared within the $|\Sigma_u \gamma\rangle$ and $|\Delta_u \gamma\rangle$ polyad blocks. In the bottom row, we show the excited eigenstates states coherently prepared within the $|A\Pi_g \gamma\rangle$ and $|X\Pi_g \gamma\rangle$ polyad blocks. The linear scale plots (left) also show a Gaussian fit to the fs VUV pump pulse spectrum. Note that within each plot, only state populations are shown for states coherently excited out of the same single initial rotational state. This is because transitions originating from different initial quantum states are not phase coherent and therefore cannot contribute to the coherent two-photons amplitudes which comprise the wavepacket signal.
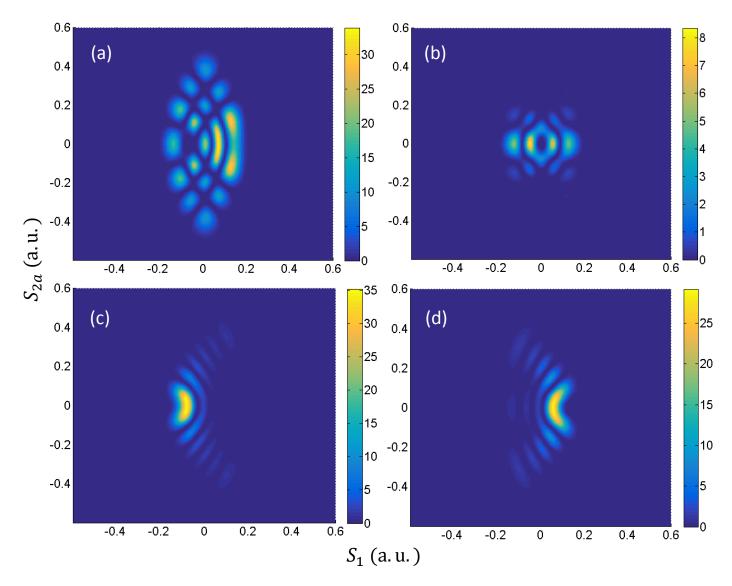
**Fig. 8** Polyad vibrational wavefunctions. The strong Fermi resonance mixing indicated in Table 1 means that the eigenstates prepared by the VUV pump pulse do not at all appear localized along normal mode coordinates. The equilibrium geometry of the $3p\sigma^2\Sigma_u$ Rydberg state is indicated as the origin in these plots. Shown are the polyad wavefunctions for eigenstates (a) $|\Sigma_u 3\rangle$ (b) $|\Delta_u 3\rangle$ (c) $|A\Pi_g 1\rangle$ (c) $|X\Pi_g 5\rangle$. The associated coherent wavepacket evolution, shown in Fig. 12, cannot be easily interpreted as motion of a classically localized Gaussian wavepacket on an excited state potential surface. For a discussion, see the text.

be accessible at the (1+2') excitation level, as discussed above, although only at the earliest pump-probe time delays, <100 fs, before long-lived zeroth-order Rydberg character is established.

It is also known that converging to each quantum state of the cation there is an associated Rydberg series. This means that there are quasi-bound neutral Rydberg (so-called superexcited) states which exist above the adiabatic Ionization Potential. Depending on electronic matrix elements and Franck-Condon factors, these Rydberg state may or may not contribute significantly to the probe absorption transition probability. If the excited electronic state to be probed has favourable Koopmans' correlations to a cation excited state, the strong absorption transition probabilities may be to Rydberg states converging to that state. However, since these are quasi-bound superexcited neutral states, a strict resonance condition applies: they must be found within the probe laser bandwidth in order to be populated. The decay of superexcited states is a well established field of research and it is generally accepted that these decay either through neutral dissociation and/or autoionization channels. Only the latter produce a free electron which would appear in a photoelectron spectrum. However, the associated kinetic energy and angular distributions are generally different from the direct photoionization channels. The direct and autoionization channels can of course interfere (with a phase shift), leading to the well known Fano line shape absorption profiles for such states. We note that within the (1+1') photoionization scheme, neither photoexcited valence states nor associated neutral photofragments are expected to be observed in our data. This is due to the (1+1') photon energy being insufficient to efficiently photoionize anything other than the 3p Rydberg manifold. Accordingly, the aforementioned direct ionisation channels are expected to provide an adequate description of the experimental TRPES data reported here. However, we additionally see in the early time data (<100 fs delays) signatures of a (1+2') process via the initially prepared $(3)^2B_2$ state, producing the Koopmans-correlated $(1)^3A_2$ electronically excited cation state. The observed <0.4 eV and ~1.6 eV photoelectron bands seen in $A_1(E)$ correspond to different regions of nuclear coordinate space (<0.4 eV at the $(3)^2B_2$ Franck-Condon region and ~1.6 eV at increased bond angles and lengths, respectively).

### 4.2.1 Direct Ionization

In our case, the $3p\sigma^2\Sigma_u$ electronic state is a member of the Rydberg series converging to the $X^1\Sigma_g$ cation ground state. Therefore, once 3p Rydberg character is developed, we expect that Koopmans-allowed direct ionization will be the major contributor to the photoionization cross section and we have no need to seek competing autoionization channels in our pump-probe data. Given that the $3p\sigma^2\Sigma_u$ electronic state has a core geometry similar to that of the cation ground state, we will assume that the latter's vibrational states can also be approximated by the Hamiltonian in Eq. 2. In other words, the final vibrational states of the cation will also have polyad structure. Each populated excited state polyad eigenstate is projected onto a manifold of continuum states by the probe pulse at a total (1+1') photon energy of 87350 cm$^{-1}$ with an effective two-photon bandwidth of 490.6 cm$^{-1}$ FWHM. The harmonic frequencies and constants required to estimate the diagonal elements of the Hamiltonian matrix are given by Jarvis *et al.*[75]. For the same reason, we can also expect transitions between corresponding polyad states in the neutral and ion to be the dominant transitions into the continuum. However, as discussed in the Introduction, due to expected non-Condon behaviour and possible small geometry changes between the 3p Rydberg state and the ground state of the cation, we also anticipate non-polyad number conserving transitions. Ionization of (5,0,0)-(0,10,0) $\Sigma_u$ polyad states is depicted in Fig. 9 with the probe and photoelectron spectra plotted for reference. In particular, a pair of pathways leading to the same final state are shown, since these are sensitive to the relative phase between the ionized polyad states. Additionally, much like in the neutral as depicted in Fig. 7, the ionic $(4,2^2,0)$-$(0,10^2,0)$ $\Delta_g$ polyad is interleaved with the (5,0,0)-(0,10,0) $\Sigma_g$ polyad resulting in energetically degenerate pathways initiating from $\Sigma_u$ and $\Delta_u$ neutral polyad states. Fig 10 shows the ionization threshold for these polyad states, as well the center two states for other $\Sigma_g$ states with the photoelectron spectrum for reference. Importantly, the stick-heights do not represent transition amplitudes and are only intended to guide the eye. The spread of the photoelectron spectrum likely indicates the non-Condon behaviour of the electronic dipole matrix element, also allowing transitions into the ionization continuum which do not conserve vibrational quanta. Similar degenerate transitions amplitudes into these final states from different coherent wavepacket states will also be induced by the probe pulse, resulting in both intra-polyad and inter-polyad interferences (quantum beats) across the photoelectron spectrum.

### 4.3 Polyad Wavepacket Dynamics

The time dependence of the TRPES signal results from photoionization of the coherent superposition of quasi-bound polyad eigenstates excited by the VUV pump pulse. Here we endeavor to explain the observed quantum beats and their decay as seen in Fig. 5(a) and (b). The quantum beats reflect the coherent evolution of the wavepacket formed by the superposition of pumped $3p\sigma^2\Sigma_u$ polyad states shown in Figs. 7. Neglecting valence and (other) Rydberg coupling to the neutral dissociative continuum, this 3p Rydberg vibrational wavepacket can be written as a superposition of polyad states

$$|\psi_{vib}(t)\rangle = \sum_{p\gamma} c_{p\gamma}(t_f) \langle v_g|p\gamma\rangle |p\gamma\rangle e^{-iE_{p\gamma}(t-t_f)/\hbar}. \tag{5}$$

The index $p$ runs over polyads which are excited coherently (out of the same initial rotational state), and $\gamma$ runs over all states within each polyad, $E_{p\gamma}$ being the energy of each state. $c_{p\gamma}(t_f)$ is the initial amplitude of each eigenstate computed by Eq. 4 and shown in Fig. 7. The wavepacket is measured by projection onto the ionization continuum at a (1+1') energy around 87,350 cm$^{-1}$ as depicted
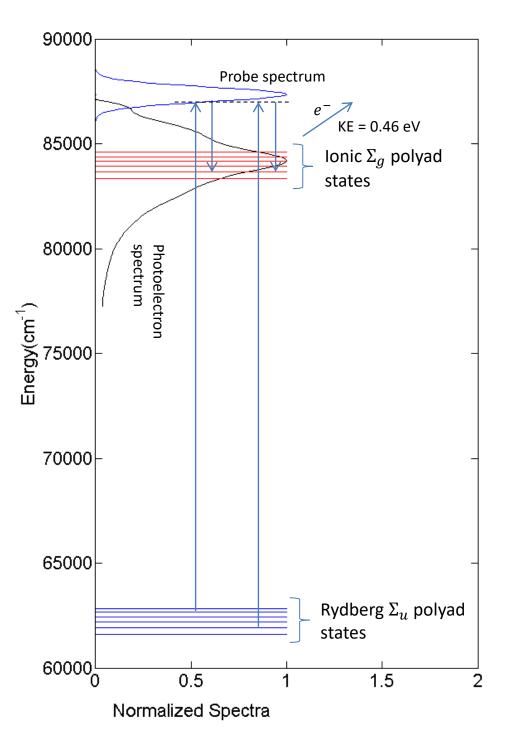
**Fig. 9** The fs UV probe pulse projects the excited state wavepacket onto the cation ground state electronic continuum as a function of time. The Probe pulse spectrum is shown as a blue curve, the observed photoelectron spectrum as a black curve. Within the Probe spectrum, an example Pump + Probe photon energy is shown as a black horizontal dashed line, with the downward arrows indicating photoelectron emission. Wavepacket signals are comprised of sets of interfering (degenerate) transition amplitudes from different coherent neutral excited states (i.e. those forming the wavepacket) to the same cation + free electron final state. As an example, we show here a schematic for the photoionization of the (5,0,0)-(0,10,0) $\Sigma_u$ polyad states, showing the interfering coherent ionization pathways. These would produce intra-polyad beats in the photoelectron signals. For a discussion, see the text.
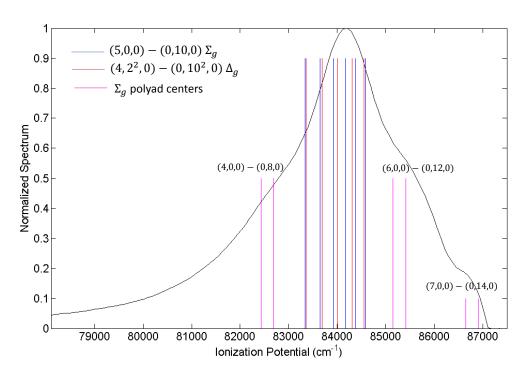
**Fig. 10** The computed cation vibrational state-resolved ionization potentials, as coloured sticks, are shown for various polyad states of the $NO_2^+$ ground state. The experimentally measured photoelectron spectrum is shown as a dotted line (black). The stick-heights do not represent transition amplitudes and are only intended to guide the eye For details, see the text.

in Fig. 9. Within the Franck-Condon approximation the ionization signal can be expressed as,

$$S(\varepsilon,t) \propto \sum_{p^+\gamma^+} |\left\langle \varepsilon X^1\Sigma_g \left| \mu_Z \right| 3p\sigma^2\Sigma_u \right\rangle \sum_{p\gamma} a_{p\gamma}(t)\tilde{E}(p^+\gamma^+,p\gamma,\varepsilon)\left\langle p^+\gamma^+|p\gamma\right\rangle|^2. \tag{6}$$

The '+' superscripts indicates ionic vibration states, $\mu_Z$ is the electronic dipole operator and $a_{p\gamma}(t) = c_{p\gamma}(t_f)\left\langle v_g|p\gamma\right\rangle e^{-iE_{p\gamma}(t-t_f)/\hbar}$ is the time dependent coefficient of $|p\gamma\rangle$ from Eq. 5. The sum ranges over all ionic polyad states correlated to energetically degenerate photoelectrons. $\tilde{E}(p^+\gamma^+,p\gamma,\varepsilon)$ is the the Fourier component of the probe pulse at the angular frequency $\left(E_{p^+\gamma^+} - E_{p\gamma} + \varepsilon\right)/\hbar$, with $\varepsilon$ being the photoelectron kinetic energy and $E_{p^+\gamma^+}, E_{p\gamma}$ being the energy of the ionic and wavepacket polyad states, respectively. The energy and coordinate dependent electronic dipole transition moment for the probe transition is unknown and left out of this equation. We are concerned here primarily with the assignment of the observed quantum beats. Therefore, with the geometry of the intermediate state and the non-Condon behaviour being unknown at present, we apply the additional drastic approximation that the FCFs are constant for each transitions out of each polyad state. While certainly inaccurate, this still provides a qualitative interpretation of beat frequencies seen in the TRPES data, as we show below. With these approximations, the above equation reduces to,

$$S(\varepsilon,t) \propto \sum_{p^+\gamma^+} |\left\langle \varepsilon X^1\Sigma_g \left| \mu_Z \right| 3p\sigma^2\Sigma_u \right\rangle \sum_{p\gamma} a_{p\gamma}(t)\tilde{E}(p^+\gamma^+,p\gamma,\varepsilon)|^2. \tag{7}$$

The sums in this equation are restricted to polyad states with degenerate pathways into continuum states correlated with an ejected electron of kinetic energy $\varepsilon$, and are (1+1') coherently excited out of the same initial ground rotational state. Importantly, transitions originating out of different initial ground quantum states are not phase coherent and therefore cannot contribute to the coherent two-photon amplitudes comprising the wavepacket signal. While calculation of the electronic dipole matrix element $\left\langle \varepsilon X^1\Sigma_g | \mu_Z | 3p\sigma^2\Sigma_u \right\rangle$ is beyond the scope of this work, for a fixed electron kinetic energy $\varepsilon$ the time dependent factor $a_{p\gamma}(t)$ and sum over vibrational states can be computed.

## 5   Discussion

We now consider the relationship between the observed TRPES signal and the underlying excited state wavepacket dynamics. In Fig. 11(a) we show the time dependent signal for the 0.07 eV peak of the experimentally observed photoelectron spectrum corresponding to the (7,0,0)-(0,14,0) ionic polyad. The calculated time dependent signal from Eq. 7 for $\varepsilon = 0.07$ eV is shown in Fig. 11(b), which shows the same oscillatory behavior as the signal at 0.07 eV but with larger contrast. A quantitative comparison cannot be made here: neither photoionization Franck-Condon factors nor the dissociative continuum (exponential population decay) part of the excited state
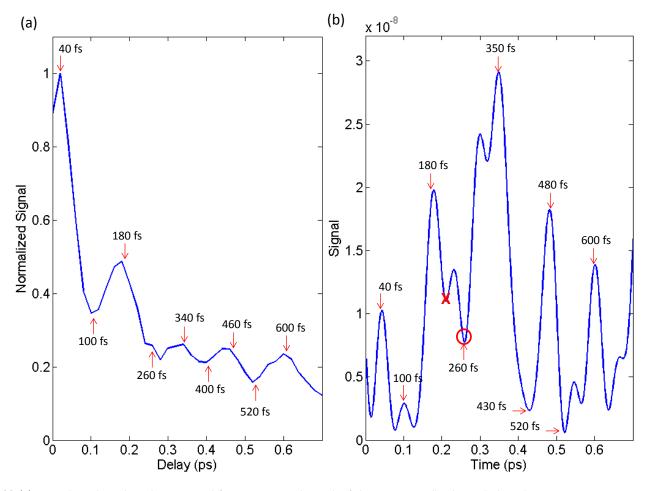
**Fig. 11** (a) Time dependent photoelectron signal for $\varepsilon = 0.07$ eV, the peak of the experimentally observed photoelectron spectrum, corresponding to transitions to the (7,0,0)-(0,14,0) ionic state polyad. (b) The calculated time dependent photoelectron signal for the (7,0,0)-(0,14,0) polyad at $\varepsilon = 0.4$ eV. The calculation shows oscillatory behavior to the signal at 0.4 eV but with larger contrast. The experimental contrast is seen to be much poorer due to (i) the limited time resolution of the experiment and (ii) the exponential damping from predissociative population decay which was not included in the calculations. For details, see the text.
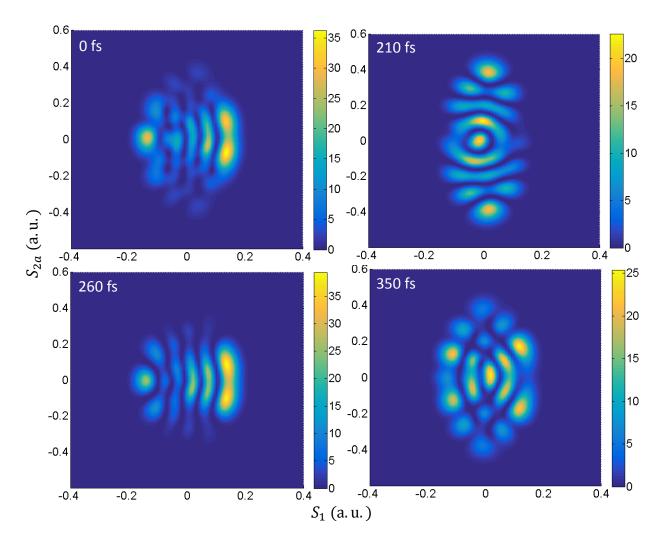
**Fig. 12** Wavepacket probability densities as a function of symmetric stretch ($S_1$) and degenerate bend ($S_{2a}$) coordinates. It can be seen that the excited state wavepacket evolution does not exhibit classical localization. Shown are the densities for the initial wavepacket (0 fs) and at time delays corresponding to 'X' (210 fs) and 'O' (260 fs) shown in Fig. 11(b), as well as that for the (calculated) signal maximum at 350 fs. See the text for details.
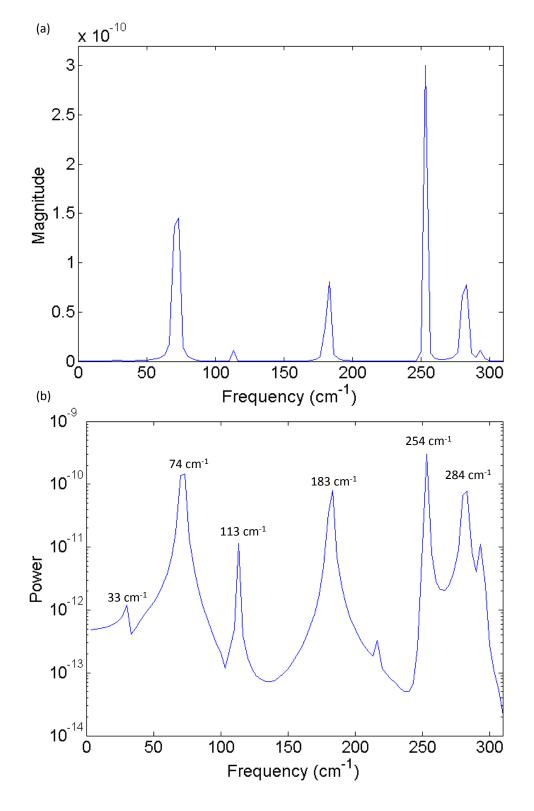
**Fig. 13** Fourier transform power spectra of the calculated $\varepsilon = 0.07$ eV photoelectron signals from Fig. 11(b), on both (a) linear and (b) logarithmic scales. These frequencies can be separated into two classes: inter-polyad and intra-polyad beats. For details, see the text.
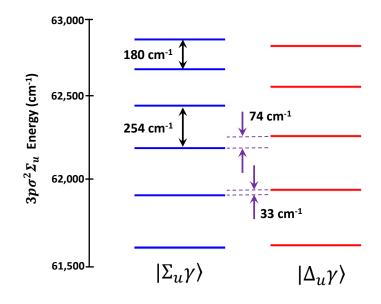
**Fig. 14** The level structure of two polyads, $\Sigma_u\gamma$ (blue) and $\Delta_u\gamma$ (red), are shown. For illustrative purposes, we show examples of intrapolyad (black arrows: 180 and 254 cm$^{-1}$) and interpolyad (purple arrows: 33 and 74 cm$^{-1}$) coherences (quantum beats) seen in both the simulations and experimental data. The assignment of all observed coherences is presented in Table 2.

nuclear wavefunction are included in the simple calculation. In our model, the variation of beat amplitude results from only the varying phases of the wavepacket eigenstates, assuming constant population. Nonetheless, we note that the locations of the experimental peaks and troughs in the data are reasonably well reproduced by the calculation. Unsurprisingly, the limited experimental time resolution and exponential population decays reduce the contrast in the experimental data. The overall population decay at longer time delays is clearly seen in the experimental data. We now consider further details of the simulation. We note two points marked by 'X' and an 'O'. The 'X' corresponds to a time delay when the population of the (0,10,0) normal mode state is near-maximal, whereas the 'O' corresponds to near-maximal (5,0,0) population. In Fig 12 we show the wavepacket density for the initial wavepacket with time delays corresponding to 'X' and 'O', as well as that for the (calculated) signal maximum at 350 fs. The peaks in the photoionization signal therefore correspond to time delays when the wavepacket most resembles the eigenstate $|\Sigma_u3\rangle$. As shown in Table 2, at these time delays the normal mode population is most thoroughly mixed. Correspondingly, the troughs in the measured signal reflect the opposite - times delays at which the wavepacket most closely resembles a pure bending or stretching mode wavefunction. This type of wavepacket evolution is reminiscent of restricted IVR, in which population oscillates back and forth between a closed set of coupled normal modes[19], with a particular normal mode dominating at specific times. The contribution of multiple, anharmonic frequencies to the experimental data is evident in Fig. 5(b). In Fig. 13 we show the Fourier transform power spectra of the calculated $\varepsilon = 0.07$ eV photoelectron signals, on both linear and log scales. While the positions and relative strengths of beat frequencies are not in precise agreement with experiment, the qualitative trends do agree (as shown in Table 2 below). The observed beat frequencies can be separated into two classes: inter-polyad and intra-polyad beats. The highest calculated frequencies are due to intra-polyad nearest neighbour beats between states comprising the (5,0,0)-(0,10,0) $\Sigma_u$ polyad. For example, the strongest contribution at 253 cm$^{-1}$ results from the (5,0,0)-(0,10,0) $\Sigma_u$ polyad beats between the states $\gamma = 3$ and 4. The strongest contribution to the experimental Fourier power spectrum, in the region spanning 200 to 250 cm$^{-1}$, can therefore be assigned to these intra-polyad beats. The calculated beat at 180 cm$^{-1}$ also originates from the (5,0,0)-(0,10,0) $\Sigma_u$ polyad, here between states $\gamma = 5$ and $\gamma = 6$. This is closest to the 151 cm$^{-1}$ beat in the experimental spectrum. Below 180 cm$^{-1}$, nearest-neighbor inter-polyad beats at 74 cm$^{-1}$, and 33 cm$^{-1}$ appear in the calculated spectrum, the 33 cm$^{-1}$ beat being many orders weaker. Experimental peaks around 84 cm$^{-1}$ and 33 cm$^{-1}$ most likely correlate to these inter-polyad beats. We note that the disagreement in the relative strengths of these beats can be ascribed to the many approximations made in the calculation: namely, the lack of kinetic energy dependent photoionization matrix elements, the lack of photoionization Franck-Condon factors, the neglect of excited neutral state population decay and limited experimental time resolution, and errors in the estimated ground-to-excited state Franck-Condon factors. Our proposed beat frequency assignments are summarized in Table 2.

In addition to the intramolecular vibrational energy redistribution between zeroth order normal mode states discussed above, we observe an overall decay of the photoionization signal, as well as in the quantum beat amplitudes shown in Fig. 5(a). This reflects both the population decay of $3p\sigma^2\Sigma_u$ state due to predissociation and the decay of the coherences between polyad eigenstates. This decay was not seen in the double-resonance spectroscopic studies of lower-lying vibrational states for which sharp rotational lines were

| Measured Beat Frequencies | Assignment(s) | Computed Level Spacings |
|---|---|---|
| 236 cm$^{-1}$±8 cm$^{-1}$ | $\Sigma_u \ \gamma = 2$ - $\gamma = 3$ | 280 cm$^{-1}$ |
|  | $\Sigma_u \ \gamma = 3$ - $\gamma = 4$ | 254 cm$^{-1}$ |
| 151 cm$^{-1}$±5 cm$^{-1}$ | $\Sigma_u \ \gamma = 5$ - $\Sigma_u \ \gamma = 6$ | 180 cm$^{-1}$ |
| 84 cm$^{-1}$±5 cm$^{-1}$ | $\Sigma_u \ \gamma = 3$ - $\Delta_u \ \gamma = 3$ | 74 cm$^{-1}$ |
| 33 cm$^{-1}$±1 cm$^{-1}$ | $\Delta_u \ \gamma = 2$ - $\Sigma_u \ \gamma = 2$ | 33 cm$^{-1}$ |

**Table 2** Experimentally observed beat frequencies and their corresponding assignments based on computed 3p polyad level spacings. The 236 and 151 cm$^{-1}$ beats are assigned to intra-polyad coherences, the 84 and 33 cm$^{-1}$ beats to inter-polyad coherences.
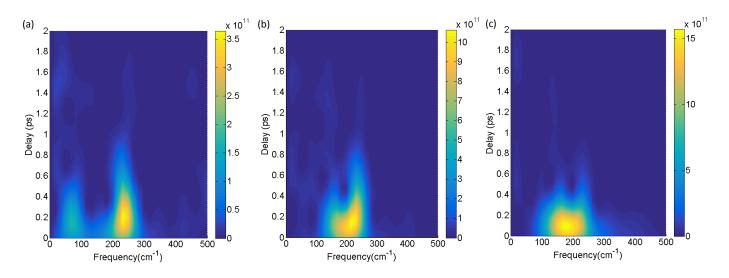


**Fig. 15** The mode-dependent coherence decay of the polyad states can be explored using spectrograms (time-windowed Fourier transforms) which show the time evolution of different beat frequencies (coherences) within the wavepacket. We show spectrograms for pump-probe photoelectron signals corresponding to the photoelectron peaks (cation final states) (a) (5,0,0)-(0,10,0), (b) (6,0,0)-(0,12,0) and (c) (7,0,0)-(0,14,0). It can clearly be seen that some coherences decay more rapidly than others. For details, see the text.

observed in the (2,0,0)-(0,4,0) and lower lying polyads[64]. In the present case, however, the degree of vibrational excitation is much higher. We also note that autoionization spectra of still higher lying electronic states in the same Rydberg series indicated that vibronic coupling, leading to vibrational autoionization, occurs via the stretching mode coordinate [66]. Remarkably, the stretching states have an order of magnitude faster autoionization rates than do the bending states. It therefore may not be coincidental that the 2D global fitting analysis of our TRPES data extracted two 3p Rydberg state decay time constants ($\tau_2$ and $\tau_3$) which differ by an order of magnitude. This suggests that the faster Rydberg state population decay seen in our data may involve coupling to valence (or other Rydberg) states via highly excited stretching and bending modes, here up to $v_1 = 5$ and $v_2 = 11$.

We note that, in general, the decay of the observed quantum beat signals in the TRPES data will comprise both population and coherence decays. In order to further investigate this, we generated spectrograms (time-windowed Fourier transforms) $S(\omega, t_0)$ for energy integrated regions of the experimental TRPES data in Fig. 5(a), here labelled $s(t)$

$$S(\omega, t_0) = \int_0^\infty e^{-(t-t_0)^2/\tau_g^2} s(t) e^{-i\omega t} dt. \tag{8}$$

A spectrogram[82] involves multiplication of the time-dependent wavepacket data $s(t)$ by a Gaussian gate function of width $\tau_g$ centered at a variable time delay $t_0$. This is then Fourier transformed, as a function of the variable time delay $t_0$, to yield a low resolution time-resolved power spectrum $S(\omega, t_0)$. The width of the gate function determines the joint frequency-time resolution. In Fig 15 (a), (b) and (c) we show spectrograms for photoelectron energy regions integrated over the (5,0,0)-(0,10,0), (6,0,0)-(0,12,0) and (7,0,0)-(0,14,0) ionic polyad manifolds, respectively. First we note that not all frequencies reported in Table 2 are observed in all three spectrograms. The intra-polyad peaks centered around 236 cm$^{-1}$ and 150 cm$^{-1}$ are present in all three spectra, whereas the 84 cm$^{-1}$ and 33 cm$^{-1}$ inter-polyad beats are observed only in the (5,0,0)-(0,10,0) spectrogram. The same is observed in the Fourier power spectrum shown in Fig. 5(b) and is likely a result of the varying overlap between the quasi-bound 3p and ionic polyad states. We note that neither the variation of Franck-Condon factors nor any non-Condon effects were included in the theoretical model. In all spectrograms, the 236 cm$^{-1}$ $\Sigma_u$ intra-polyad beat has an apparently slower initial coherence decay time. The 150 cm$^{-1}$ assigned to a $\Sigma_u$ intra-polyad beat has an apparently faster initial coherence decay time, as does the $\Sigma_u$-$\Delta_u$ inter-polyad beat. The latter, however, exhibits a coherence revival (vide infra). There is a variation of coherence decay time within the $\Sigma_u$ polyad. We specifically note that the higher lying states
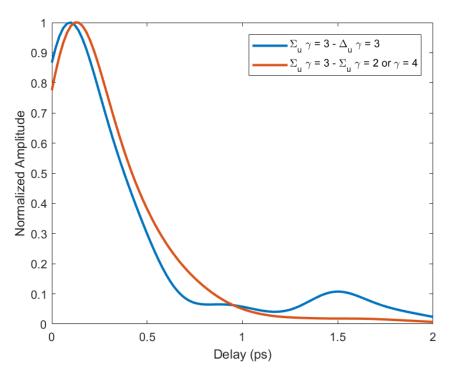
**Fig. 16** Time-dependent coherence amplitudes for an intra-polyad (236 cm$^{-1}$) and an inter-polyad (74 cm$^{-1}$) region from the experimental spectrogram in Fig. 15(a). The inter-polyad coherence (blue) shows faster initial decay with a revival in amplitude at around 1.5 ps time delay. The intra-polyad coherence (red) shows no revival. This is related to vibrational state specificity in the predissociation dynamics. See the text for further discussion.

- $\Sigma_u$ $\gamma = 5,6$ - assigned to the 150 cm$^{-1}$ beat - exhibit faster initial coherence decays than do the lower lying states. The observed faster initial decay of the inter-polyad beat suggests that the (4,2$^2$,2)-(0,10$^2$,0) $\Delta_u$ polyad states may have a faster coherence decay rate than do the (5,0,0)-(0,10,0) $\Sigma_u$ states. However, as shown below, the appearance of a coherence revival requires further investigation. To this end, we integrated over frequency regions of the spectrogram corresponding to the inter-polyad (74 cm$^{-1}$) and intra-polyad (236 cm$^{-1}$) beats in Fig 15(a) and plotted these as a function of time in Fig 16. The time dependence of both the inter-polyad (red) and intra-polyad (blue) coherences are shown. Interestingly, we observe a revival in the amplitude of the $\Sigma_u$-$\Delta_u$ inter-polyad beat, suggesting that it is actually longer lived. We further note that, out of all the 3p polyads, only the $\Delta_u$ states comprise basis states containing two units of projection of the bending vibrational angular momentum. The Rydberg electronic character associated with these $\Delta_u$ polyad vibrational states may be different from those with zero projection bend angular momentum. This is equivalent to suggesting that there may be multi-configurational mixing which is Rydberg vibrational mode dependent. Therefore, in addition to different predissociative linewidths, we also expect that the molecular vibronic eigenstates associated with the $\Delta_u$ polyad will have an electronic character differing from those of the $\Sigma_u$ polyad. We speculate that the observed inter-polyad coherence revival could potentially be explained by variation of the zeroth-order electronic character of the wavepacket between valence and $3p\sigma^2\Sigma_u$ Rydberg states, since only the latter can be directly ionized and detected in our experiment. Within a Born-Oppenheimer basis, this is equivalent to a vibrational angular momentum dependent nonadiabatic coupling between the 3p Rydberg and valence (or other Rydberg) electronic states. In this picture, the vibrational wavepacket decoheres and revives on a timescale commensurate with the electronic motion. Further experiments and/or calculations will be needed to verify this hypothesis.

## 6    Summary and Outlook

We reported on a TRPES study of vibronic wavepacket dynamics in the triatomic NO$_2$ excited with a fs VUV pump pulse centred at 160.4 nm (7.73 eV). In this region, the optically 'bright' zeroth-order $^2B_2$ valence state rapidly dephases into the relatively long-lived zeroth-order $3p\sigma^2\Sigma_u$ Rydberg state, a member of the Rydberg series converging to the ground electronic state of the cation. Due to both Koopmans correlations and Franck-Condon overlaps, our TRPES scheme selectively monitors dynamics within the zeroth-order $3p\sigma^2\Sigma_u$ Rydberg state. Vibrational dynamics within the 3p state evolved under the influence of strong multimodal anharmonic Fermi resonance coupling, meaning that the 3p vibrational states are best described as polyads and that the usual normal mode picture of vibrational dynamics and their coupling fails completely. We observed final cation state dependent quantum beats whose frequencies could be assigned to $3p\sigma^2\Sigma_u$ polyad level spacings determined from an effective spectroscopic Hamiltonian, one which does not include predissociation. This in turn indicates that the zeroth-order 3p state serves as a good description for the vibrational wavepacket dynamics

seen here. We could assign the observed quantum beats to the calculated intra-polyad and inter-polyad coherences, confirming the origin of this photoelectron signal. The polyad structure of the vibrational wavefunctions suggests that the vibrational wavepacket dynamics in the 3p Rydberg state is highly complex and cannot be interpreted as energy flow between normal modes and precludes therefore any simple (i.e. semiclassical) molecular movies. The wavepacket evolution pictured in Fig. 12 is a both a vivid representation of restricted IVR and a challenge to the Molecular Movie concept.

Coupling of the zeroth-order state $3p\sigma^2\Sigma_u$ Rydberg state to other electronic states is observed as a global decay in the photoionization signal, modeled by Eq. 3, and by decays in the coherence amplitudes such as exemplified by Fig. 16. The global decay of the TRPES signals indicate that there is a perturbative (i.e. weak relative to Fermi resonance couplings) nonadiabatic Rydberg-valence and/or Rydberg-Rydberg coupling leading to predissociation and the formation of free atomic and molecular fragments. In this perturbative picture, weak coupling to a dissociation continuum adds a decay linewidth to each polyad state but does not significantly shift its energy. That the predissociation rates are slower than vibrational coupling time scales is evidenced from our ability to assign the observed quantum beats to level spacings of the effective Hamiltonian which includes no predissociation. Global fitting of the TRPES data revealed that three statistically significant time constants, $\tau_1 = 77$ fs, $\tau_2 = 0.45$ ps and $\tau_3 = 5.4$ ps, are required to describe the data. The Decay Associated Spectra correlated with these time constants, $A_1(E)$, $A_2(E)$ and $A_3(E)$, suggest a kinetic model comprising a sequential followed by a parallel signal decay. The negative amplitude seen in $A_1(E)$ forces a sequential model for the first step. We interpret this as the initially prepared (by the fs VUV pump pulse) zeroth-order state having dominant $^2B_2$ valence character which quickly ($\tau_1$) dephases into zeroth-order $3p\sigma^2\Sigma_u$ Rydberg character. The expected large geometry change between the $^2B_2$ valence state and the cation ground state is consistent with the $A_1(E)$ photoelectron spectrum being peaked towards zero kinetic energy and displaying an ancillary (1+2') peak occurring at ~1.6 eV electron kinetic energies. The negative peak at 0.4 eV in the sequential kinetics fit indicates that the configurations $A_2(E)$ and $A_3(E)$, formed via rapid (cross-correlation limited) decay of the initial $^2B_2$ valence state, have photoelectron bands with maxima at around 0.4 eV. Using the effective Hamiltonian, we assigned this photoelectron band to the photoionization of polyads in the zeroth-order $3p\sigma^2\Sigma_u$ Rydberg state to the analogous (but not identical) polyads in the cation ground state. It is interesting that the two DAS $A_2(E)$ and $A_3(E)$ have very similar forms (indicating no significant change in geometry) and that $A_2(E)$ contains no negative amplitudes. This means that we cannot interpret the decay constant $\tau_2$ as being part of a sequential kinetic process. This leaves the remaining possibility that the $3p\sigma^2\Sigma_u$ Rydberg state 'impulsively' formed via rapid dephasing from the zeroth-order $^2B_2$ configuration may generate two geometrically similar ($A_2(E)$ and $A_3(E)$) but distinct populations which independently decay on their own (distinct) time scales ($\tau_2$ and $\tau_2$) to an undetected state. The latter we presume to lead directly to free atomic and molecular fragment predissociation products. We speculate that the order of magnitude difference in decay rates seen for these kinetically distinct populations must be associated with differences in the Rydberg electronic component of their associated wavefunction, rather than in their vibrational structure. It is interesting to note that order-of-magnitude differences in mode-specific autoionization rates were previously observed for a higher lying member (n=14) of the same $3p\sigma^2\Sigma_u$ Rydberg series[83]. By comparing 3p (n=14) autoionization linewidths for (100) with (010) vibrational states, it was concluded that the symmetric stretch coordinate couples about ten times more strongly with Rydberg electron orbital motion than does the bend.

Using spectrograms (time-windowed Fourier transforms), we analyzed the time dependence of the observed coherences between polyad states. As seen in Fig. 16, we observed that (i) the 74 cm$^{-1}$ inter-polyad coherence ($\Sigma_u\gamma=3$ - $\Delta_u\gamma=3$) persists longer (with a revival at 1.5 ps) than does the 236 cm$^{-1}$ intra-polyad coherence ($\Sigma_u\gamma=3$ - $\Sigma_u\gamma=2$ or 4) and (ii) that within a polyad (e.g. $\Sigma_u$) the coherences between higher energy members (e.g. $\gamma=5,6$) decay more rapidly than do the lower energy members (e.g. $\gamma=2$-4). Within the perturbative weak coupling predissociation picture, we can assign an individual decay lifetime to each individual polyad (scattering resonance) state. In this perturbative limit, the decay of a coherence amplitude arising from any such pair will have a decay rate equal to the product of the decay rates of the individual predissociation resonances[55]. We can therefore speculate slightly further as to these observed differences in coherence decays. The 74 cm$^{-1}$ and 236 cm$^{-1}$ coherences share one polyad in common, namely $\Sigma_u$ $\gamma=3$. This implies that the observed differences in coherence decays must be due to the other state forming the coherence. Thus, the $\Delta_u$ $\gamma=3$ polyad must be longer lived (i.e. slower predissociation rate) than are the $\Sigma_u$ $\gamma=2$ or 4 polyad states. We note that the $\Delta_u$ $\gamma=3$ polyad contains two units of projection of the bend angular momentum, absent in the $\Sigma_u$ polyads. If this is correlated with a change in the associated 3p Rydberg electronic wavefunction, we speculate that there may be an electronic origin to slower predissociative coupling for this state. This will require more detailed investigation. From a more general perspective, the coherence amplitude decays emerge as a result of decay rates associated with the underlying density matrix elements in the zero-order basis[84]. As discussed in[74], the TRPES signal is a linear superposition of multipole moments built from the density matrix. Therefore, an analysis of these data using such multipole moments could provide an estimate of the decay rates associated with various density matrix elements, providing an experimental indicator of the strength of various nonadiabatic coupling channels. Work towards this level of data analysis is currently underway.

In sum, the excited state wavepacket dynamics of polyatomic molecules will generally include nonadiabatic (vibronic) dynamics, photodissociation, and multimode anharmonic vibrational resonances which, in the restricted IVR regime, lead to the formation of polyads. As shown here for the case of $NO_2$, the structural/vibrational dynamics associated with such wavepackets is inherently quantum mechanical in nature: semiclassical molecular movie visualizations of a 'structure evolving as a function of time' may not apply. The complex drama of VUV-excited $NO_2$ is indeed a Quantum Molecular Movie.

## Conflicts of interest

There are no conflicts to declare.

## Acknowledgements

## Notes and references

1   A. Stolow, *Faraday Discussions*, 2013, **163**, 9–32.
2   D. Huber and E. J. Heller, *The Journal of chemical physics*, 1987, **87**, 5302–5311.
3   *Structural Dynamics*, `ttps://aca.scitation.org/sdy/info/focus`.
4   J. R. Dwyer, C. T. Hebeisen, R. Ernstorfer, M. Harb, V. B. Deyirmenjian, R. E. Jordan and R. Dwayne Miller, *Philosophical Transactions of the Royal Society A: Mathematical, Physical and Engineering Sciences*, 2006, **364**, 741–778.
5   A. A. Ischenko, P. M. Weber and R. D. Miller, *Chemical reviews*, 2017, **117**, 11066–11124.
6   J. Yang, M. Guehr, X. Shen, R. Li, T. Vecchione, R. Coffee, J. Corbett, A. Fry, N. Hartmann, C. Hast *et al.*, *Physical review letters*, 2016, **117**, 153002.
7   J. Glownia, A. Natan, J. Cryan, R. Hartsock, M. Kozina, M. Minitti, S. Nelson, J. Robinson, T. Sato, T. van Driel *et al.*, *Physical review letters*, 2016, **117**, 153003.
8   J. Yang, X. Zhu, T. J. Wolf, Z. Li, J. P. F. Nunes, R. Coffee, J. P. Cryan, M. Gühr, K. Hegazy, T. F. Heinz *et al.*, *Science*, 2018, **361**, 64–67.
9   T. J. Wolf, D. Sanchez, J. Yang, R. Parrish, J. Nunes, M. Centurion, R. Coffee, J. Cryan, M. Gühr, K. Hegazy *et al.*, *Nature chemistry*, 2019, **11**, 504–509.
10  T. Uzer and W. Miller, *Physics Reports*, 1991, **199**, 73–146.
11  J. C. Keske and B. H. Pate, *Annual review of physical chemistry*, 2000, **51**, 323–353.
12  M. Gruebele, *Advances in Chemical Physics*, 2000, **114**, 193–262.
13  M. Gruebele and P. G. Wolynes, *Accounts of chemical research*, 2004, **37**, 261–267.
14  D. M. Leitner, *Advances in Physics*, 2015, **64**, 445–517.
15  H.-R. Dübal and M. Quack, *Molecular Physics*, 1984, **53**, 257–264.
16  J. Baggott, M.-C. Chuang, R. N. Zare, H. Dübal and M. Quack, *The Journal of chemical physics*, 1985, **82**, 1186–1194.
17  S. A. B. Solina, J. P. O'Brie, R. W. Field and W. F. Polik, *The Journal of Physical Chemistry*, 1996, **100**, 7797–7809.
18  M. Joyeux, S. Y. Grebenshchikov and R. Schinke, *The Journal of chemical physics*, 1998, **109**, 8342–8354.
19  P. M. Felker and A. H. Zewail, *Physical review letters*, 1984, **53**, 501.
20  L. Bigio and E. R. Grant, *The Journal of Chemical Physics*, 1985, **83**, 5361–5368.
21  D. R. Borst and D. W. Pratt, *The Journal of Chemical Physics*, 2000, **113**, 3658–3669.
22  K. L. Reid, *International Reviews in Physical Chemistry*, 2008, **27**, 607–628.
23  D. J. Nesbitt and R. W. Field, *The Journal of Physical Chemistry*, 1996, **100**, 12735–12756.
24  E. Fermi, *Zeitschrift für Physik*, 1931, **71**, 250–259.
25  G. Amat and M. Pimbert, *Journal of Molecular Spectroscopy*, 1965, **16**, 278–290.
26  H. E. Howard-Lock and B. Stoicheff, *Journal of Molecular Spectroscopy*, 1971, **37**, 321–326.
27  D. T. Colbert and E. L. Sibert III, *The Journal of chemical physics*, 1989, **91**, 350–363.
28  P. M. Felker and A. H. Zewail, *The Journal of chemical physics*, 1985, **82**, 2961–2974.
29  P. M. Felker and A. H. Zewail, *The Journal of chemical physics*, 1985, **82**, 2975–2993.
30  M. Herman and D. S. Perry, *Physical Chemistry Chemical Physics*, 2013, **15**, 9970–9993.
31  P. M. Felker and A. H. Zewail, *The Journal of chemical physics*, 1985, **82**, 2994–3002.
32  P. M. Felker, W. R. Lambert and A. H. Zewail, *The Journal of chemical physics*, 1985, **82**, 3003–3010.
33  A. Stolow and J. G. Underwood, *Advances in Chemical Physics*, 2008, **139**, 497–583.
34  J. Smith, C. Lakshminarayan and J. Knee, *The Journal of Chemical Physics*, 1990, **93**, 4475–4476.
35  A. K. King, S. M. Bellm, C. J. Hammond, K. L. Reid, M. Towrie and P. Matousek, *Molecular Physics*, 2005, **103**, 1821–1827.
36  C. J. Hammond, K. L. Reid and K. L. Ronayne, *The Journal of Chemical Physics*, 2006, **124**, 201102.
37  J. A. Davies and K. L. Reid, *The Journal of chemical physics*, 2011, **135**, 124305.

38  H. Köppel, W. Domcke and L. S. Cederbaum, *Advances in chemical physics*, 1984, **57**, 59–246.

39  M. Klessinger and J. Michl, *Excited states and photochemistry of organic molecules*, VCH publishers, 1995.

40  M. Ben-Nun, J. Quenneville and T. J. Martínez, *The Journal of Physical Chemistry A*, 2000, **104**, 5161–5175.

41  G. A. Worth and L. S. Cederbaum, *Annu. Rev. Phys. Chem.*, 2004, **55**, 127–158.

42  W. Domcke, D. Yarkony and H. Köppel, *Conical intersections: electronic structure, dynamics & spectroscopy*, World Scientific, 2004, vol. 15.

43  W. Domcke, D. R. Yarkony and H. Köppel, *Conical intersections: theory, computation and experiment*, World Scientific, 2011, vol. 17.

44  A. L. Thompson and T. J. Martínez, *Faraday discussions*, 2011, **150**, 293–311.

45  H. H. Fielding and G. A. Worth, *Chemical Society Reviews*, 2018, **47**, 309–321.

46  S. Adachi, T. Schatteburg, A. Humeniuk, R. Mitrić and T. Suzuki, *Physical Chemistry Chemical Physics*, 2019, **21**, 13902–13905.

47  H. R. Hudock, B. G. Levine, A. L. Thompson, H. Satzger, D. Townsend, N. Gador, S. Ullrich, A. Stolow and T. J. Martinez, *The Journal of Physical Chemistry A*, 2007, **111**, 8500–8508.

48  W. J. Glover, T. Mori, M. S. Schuurman, A. E. Boguslavskiy, O. Schalk, A. Stolow and T. J. Martínez, *The Journal of chemical physics*, 2018, **148**, 164303.

49  M. S. Schuurman and A. Stolow, *Annual review of physical chemistry*, 2018, **69**, 427–450.

50  R. Schinke, *Photodissociation dynamics: spectroscopy and fragmentation of small polyatomic molecules*, Cambridge University Press, 1995.

51  M. Shapiro and R. Bersohn, *Annual Review of Physical Chemistry*, 1982, **33**, 409–442.

52  P. Brumer and M. Shapiro, *Adv. Chem. Phys*, 1985, **60**, 371.

53  G. Balint-Kurti and M. Shapiro, *Advances in Chemical Physics*, 1985, **60**, 403.

54  G. Herzberg, *Electronic spectra and electronic structure of polyatomic molecules*, Krieger Publishing Company, 1991, vol. 2.

55  M. Shapiro, M. J. Vrakking and A. Stolow, *The Journal of chemical physics*, 1999, **110**, 2465–2473.

56  I. Wilkinson and B. J. Whitaker, *Annual Reports Progress Chemistry, Section" C"(Physical Chemistry)*, 2010, **106**, 274–304.

57  J. W. Au and C. Brion, *Chemical physics*, 1997, **218**, 109–126.

58  I. D. Petsalakis, G. Theodorakopoulos and M. S. Child, *The Journal of Chemical Physics*, 2001, **115**, 10394–10403.

59  R. Ritchie and A. Walsh, *Proceedings of the Royal Society of London A: Mathematical, Physical and Engineering Sciences*, 1962, **267**, 395–407.

60  K. Haber, J. Zwanziger, F. Campos, R. Wiedmann and E. Grant, *Chemical physics letters*, 1988, **144**, 58–64.

61  R. S. Tapper, R. L. Whetten, G. S. Ezra and E. R. Grant, *The Journal of Physical Chemistry*, 1984, **88**, 1273–1275.

62  M. Taherian, P. Cosby and T. Slanger, *Journal of Physical Chemistry*, 1987, **91**, 2304–2309.

63  I. Wilkinson, I. A. Garcia, B. J. Whitaker, J.-B. Hamard and V. Blanchet, *Physical Chemistry Chemical Physics*, 2010, **12**, 15766–15779.

64  H. Matsui, E. E. Mayer and E. R. Grant, *Journal of Molecular Spectroscopy*, 1996, **175**, 203–214.

65  M. Child, *Theory of Molecular Rydberg States*, Cambridge University Press, 2011.

66  G. P. Bryant, Y. Jiang and E. R. Grant, *The Journal of chemical physics*, 1992, **96**, 4827–4840.

67  R. Forbes, V. Makhija, K. Veyrinas, A. Stolow, J. W. Lee, M. Burt, M. Brouard, C. Vallance, I. Wilkinson, R. Lausten *et al.*, *The Journal of Chemical Physics*, 2017, **147**, 013911.

68  M. R. Coates, M. A. B. Larsen, R. Forbes, S. P. Neville, A. E. Boguslavskiy, I. Wilkinson, T. I. Sølling, R. Lausten, A. Stolow and M. S. Schuurman, *The Journal of Chemical Physics*, 2018, **149**, 144311.

69  M. Beutler, M. Ghotbi, F. Noack and I. V. Hertel, *Optics letters*, 2010, **35**, 1491–1493.

70  M. Ghotbi, M. Beutler and F. Noack, *Optics letters*, 2010, **35**, 3492–3494.

71  U. Even, *EPJ Techniques and Instrumentation*, 2015, **2**, 17.

72  C. Z. Bisgaard, O. J. Clarkin, G. Wu, A. M. Lee, O. Geßner, C. C. Hayden and A. Stolow, *Science*, 2009, **323**, 1464–1468.

73  P. Hockett, C. Z. Bisgaard, O. J. Clarkin and A. Stolow, *Nature Physics*, 2011, **7**, 612–615.

74  V. Makhija, K. Veyrinas, A. E. Boguslavskiy, R. Forbes, I. Wilkinson, R. Lausten, S. P. Neville, S. T. Pratt, M. S. Schuurman and A. Stolow, *Journal of Physics B: Atomic, Molecular and Optical Physics*, 2020, **53**, 114001.

75  G. Jarvis, S. Y., N. C.Y. and E. Grant, *Journal of Chemical Physics*, 1999, **111**, 9568.

76  A. E. Boguslavskiy, M. S. Schuurman, D. Townsend and A. Stolow, *Faraday discussions*, 2011, **150**, 419–438.

77  D. M. Hirst, *The Journal of Chemical Physics*, 2001, **115**, 9320.

78  B. Kirmse, A. Delon and R. Jost, *The Journal of Chemical Physics*, 1998, **108**, 6638.

79  K. P. Huber and G. Herzberg, *Molecular Spectra and Molecular Structure IV. Constants of Diatomic Molecules*, Van Nostrand Reinhold Company Inc., 1979.

80  T. Nakayama, M. Y. Kitamura and K. Watanabe, *The Journal of Chemical Physics*, 1959, **30**, 1180–1186.

81 P. Bell, F. Aguirre, E. Grant and S. Pratt, *The Journal of chemical physics*, 2003, **119**, 10146–10157.

82 I. Fischer, M. J. Vrakking, D. Villeneuve and A. Stolow, *Chemical physics*, 1996, **207**, 331–354.

83 F. X. Campos, Y. Jiang and E. R. Grant, *The Journal of chemical physics*, 1990, **93**, 7731–7739.

84 V. May and O. Kühn, *Charge and energy transfer dynamics in molecular systems*, John Wiley & Sons, 2008.